Planet formation through the lens of dynamics

Huang, S.

2

When, where, and how many exoplanets end up in orbital resonances?

The theory of Type I migration has been widely used in many studies. Transiting multi-planet systems offer us the opportunity to examine the consistency between observation and theory, especially for those systems harbouring planets in Mean Motion Resonance (MMR). The displacement these resonant pairs show from exact commensurability provides us with information on their migration and eccentricity-damping histories. Here, we adopt a probabilistic approach, characterized by two distributions – appropriate for either the resonant or non-resonant planets – to fit the observed planet period ratio distribution. With the Markov chain Monte Carlo (MCMC) method, we find that ≈15% of exoplanets are in first order (j+1:j) MMRs, the ratio of eccentricity-to-semi-major axis damping is too high to allow overstable librations and that the results are by-and-large consistent with Type-I migration theory. In addition, our modeling finds that a small fraction of resonant pairs is captured into resonance during migration, implying late planet formation (gas-poor). Most of the resonant pairs park themselves at the migration barrier, indicating early planet formation (gas-rich). Furthermore, after improving the criterion on two-body resonant trapping, we obtain an upper limit of the disc surface density at the time the planets are locked in resonance.

S. Huang★, C. W. Ormel (2023) When, where, and how many planets end up in first-order resonances? MNRAS, 522, 828

2.1 Introduction

Since the first discovery of exoplanets around solar-type stars (Mayor & Queloz 1995), the number of exoplanets has ballooned in the last three decades, exceeding 5 200 as of the present day. It is therefore appropriate to conduct population-level analyses to examine planet formation theories (Mordasini et al. 2015; Zhu & Dong 2021). When independent mass and radius measurements are available, planet bulk density and their composition can be inferred (Fortney et al. 2007; Seager et al. 2007; Piaulet et al. 2022), with which their mass accretion history and post-formation evolution can be constrained. The core accretion model successfully predicted the so-called "planet dessert" (Ida & Lin 2004), which refers to the paucity of planets with tens of Earth-mass within 3 au. The "radius valley" (Fulton et al. 2017) is manifested at a planet radius $\sim 2R_\oplus$, which has been attributed to photoevaporation-driven mass loss (Owen & Wu 2013, 2017), planet formation location with respect to snow line (Luque & Pallé 2022; Izidoro et al. 2022), or core-powered mass loss (Ginzburg et al. 2018).

The physical principles underlying migration of low-mass planets in gaseous discs (Type I migration) have long been established (Goldreich & Tremaine 1979; Lin & Papaloizou 1979). The total torque exerted on planets by the surrounding disc is typically negative, resulting in inward planet migration on time-scales shorter than the disc lifetimes (e.g., Ward 1997; Tanaka et al. 2002; Ribas et al. 2014; Winter et al. 2019). However, the direction of migration can be reversed at special locations where conditions materialize that render a net positive torque, resulting in migration traps. These locations include the region where the horseshoe saturates, i.e when the (positive) co-rotation torque compensates the (negative) Lindblad torque (Goldreich & Tremaine 1980; Ward 1991; Paardekooper et al. 2010, 2011), the disc inner edge (Liu et al. 2017; Romanova et al. 2019; Ataiee & Kley 2021) where the torque becomes one-sided, and the regions where the disc switches from optically thin to optically thick (0.1 – 1 au) (Masset et al. 2006). In addition, in the pebble accretion paradigm, the infalling dust can efficiently induce (positive) thermal torque onto the planets (Benítez-Llambay et al. 2015; Masset 2017; Guilera et al. 2019, 2021).

Although the present close-in positions of exoplanets indirectly hint at planet migration, it is hard to quantitatively test the theory based only on single-planet systems. Instead, multi-planet systems, especially those with planet pairs in Mean Motion Resonance (MMR) leave richer dynamical imprints against which the theory can be tested (Snellgrove et al. 2001; Papaloizou & Szuszkiewicz 2005). It is likely that such resonant architecture results from migration in a gas-rich environment (i.e., the disc) as energy dissipation is needed to trap planets in resonance (Terquem & Papaloizou 2007; Raymond et al. 2008; Rein 2012; Batygin 2015). One famous example is PDS 70, which harbours two directly imaged near-resonance planets in its protoplanetary disc (Bae et al. 2019; Benisty et al. 2021). Besides, a chain of planets in resonance might sculpt the asymmetry disc structure in HD 163296 (Isella et al. 2018; Garrido-Deutelmoser et al. 2023a). In particular, there tends to be an excess of systems with planets' period ratio just wide of commensurability (Fabrycky et al. 2014; Steffen & Hwang 2015), indicating that a certain fraction of planet pairs are truly in resonance.

Formally, two planets are said to be in $(j+1) : j$ resonance if at least one of their resonance angles ($\phi_{1,2} = (j+1)\lambda_2 - j\lambda_1 - \varpi_{1,2}$, with λ_i the mean longitudes and ϖ_i the longitude of pericentres) librate around a fixed value. However, the values of the resonance angles are poorly constrained because it is hard to constrain ϖ_i for near-circular orbits. We therefore

turn our attention to their period ratios and define the dimensionless parameter

$$\Delta = \frac{P_2}{P_1} - \frac{j+1}{j} \tag{2.1}$$

to measure the offset of the period ratio away from a first-order $(j+1) : j$ commensurability. Here, P_1 is the period of the inner planet and P_2 that of the outer. If two planets are in a $(j+1) : j$ resonance, the offset Δ must be close to zero. Xie (2014) and Ramos et al. (2017) emphasize that the exact value of Δ is determined by migration and eccentricity damping, linking the observed quantity Δ to planet migration (Charalambous et al. 2022). It offers us an opportunity to examine planet-disc interaction histories through planets in MMR in multi-planet systems. The migration history of such specific multi-planet systems like TRAPPIST-1 (Gillon et al. 2017; Luger et al. 2017; Huang & Ormel 2022), K2-24 (Petigura et al. 2018; Teyssandier & Libert 2020) and TOI-1136 (Dai et al. 2022), can be reconstructed.

Yet, most exoplanets are obviously not in resonance because of their large offsets Δ. Various scenarios have been proposed to explain the overall observed non-resonant planetary architecture statistically. These include dynamical instability (Izidoro et al. 2017, 2021), disc winds (Ogihara et al. 2018), *in situ* formation of sub-Netunes (Dawson et al. 2015; Choksi & Chiang 2020), planetesimal scattering (Chatterjee & Ford 2015; Ghosh & Chatterjee 2022), stellar tides (Lithwick & Wu 2012; Delisle & Laskar 2014; Xie 2014; Sánchez et al. 2020), and stochastic forces (Rein & Papaloizou 2009; Goldberg & Batygin 2022). However, many of these works introduce additional free parameters in order to match the only observed quantity – the period ratio distribution. Overfitting may occur. One way to improve on this is to include more observational quantities. For example, Goldberg & Batygin (2022) and Choksi & Chiang (2022) find that by additionally accounting for the TTV signatures of hundreds of Kepler planets, a laminar disc alone cannot reproduce the observed TTV features. Either additional planets (perturbers) are required (Choksi & Chiang 2022) or their birth proto-discs are turbulent (Goldberg & Batygin 2022).

In this work, we introduce a statistical approach to study all transiting exoplanets and try to answer when, where, and how many planets are captured in resonance. The observed planetary radii, orbital periods, and host stellar masses are taken into account. By assuming that the period ratio distribution is characterized by two distributions, representing both resonant and non-resonant planets, the probability that a planets pair is in resonance is evaluated. Whether the migration and eccentricity damping is consistent with migration theory is determined. In addition, our approach allows us to constrain the timing and the location, of the resonance trapping, which implies the pathway of planet formation.

The paper is structured as follows: We first introduce our statistical model in Sect. 2.2. Using the MCMC method, we constrain the relation between eccentricity damping time-scale and migration time-scale in Sect. 2.4. Along with the resonance trapping criterion that we improve on (Sect. 2.3), we address when, where, and how many planets are in resonance Sect. 2.5. The discussion and conclusion of this study are presented in Sect. 2.6 and Sect. 2.7, respectively.

2.2 Methodology

In this section, we describe our disc model and migration (Type I), and construct the likelihood function needed for the Monte Carlo Markov Chain (MCMC) simulations of Sect. 2.4. Since our migration model is linear with planet mass (Type I), we focus on the planets with relatively low planet-to-star mass ratios which are not likely to open a gap when they are in

the protoplanet disc. We assume that the relevant disc quantities follow power-law distribution (Sect. 2.2.1). We describe the migration model in Sect. 2.2.2. The equilibrium dynamics of planets trapping in resonance are described in Sect. 2.2.3. The masses of observed planets are calculated from a mass-radius (M-R) relationship. Its prescription is given in Sect. 2.2.4. The total log-likelihood function we construct for the MCMC is detailed in Sect. 2.2.5.

2.2.1 Disc model

As most observed transiting planets are located within ∼1 au of their host star, we will describe the possible structures of the inner disc. We assume that the gas surface density always follows a power-law distribution:

$$\Sigma(r) = \Sigma_{1\mathrm{au}} \left(\frac{r}{1\,\mathrm{au}}\right)^{s}, \tag{2.2}$$

where $\Sigma_{1\mathrm{au}}$ is the gas surface density at 1 au and s is its slope. The gas aspect ratio also follows a power-law distribution:

$$h(r) = h_{1\mathrm{au}} \left(\frac{r}{1\,\mathrm{au}}\right)^{q} \tag{2.3}$$

where $h_{1\mathrm{au}}$ is the gas aspect ratio at 1 au and q is its slope. Different assumptions about the disc structure, e.g., heating mechanisms, result in distinct values of s, q, $\Sigma_{1\mathrm{au}}$, and $h_{1\mathrm{au}}$. Typically, the inner disc is optically thick and the main heating energy comes from viscous dissipation (Ruden & Lin 1986), while the outer disc is optically thin and stellar irradiation mainly heat the disc onto its surface layer (Chiang & Goldreich 1997).

For discs dominated by stellar radiation, we make use of the disc structure from Liu et al. (2019). The gas surface density is:

$$\Sigma_{\mathrm{g,irr}} = 250 \left(\frac{\dot{M}_g}{10^{-8} M_\odot/\mathrm{yr}}\right) \left(\frac{M_\star}{M_\odot}\right)^{\frac{9}{14}} \left(\frac{L_\star}{L_\odot}\right)^{-\frac{2}{7}} \left(\frac{r}{\mathrm{au}}\right)^{-\frac{15}{14}} \mathrm{g\,cm^{-2}} \tag{2.4}$$

where $\dot{M}_g$ is stellar accretion rate and $L_\star$ is the star luminosity. The aspect ratio is:

$$h_{\mathrm{g,irr}} = 0.0245 \left(\frac{M_\star}{1 M_\odot}\right)^{-4/7} \left(\frac{L_\star}{1 L_\odot}\right)^{1/7} \left(\frac{r}{1\,\mathrm{au}}\right)^{2/7}. \tag{2.5}$$

For stars of mass between $0.43 M_\odot$ and $2 M_\odot$, which covers most of our star sample, the mass-luminosity relation is well represented by $L_\star/L_\odot = (M_\star/M_\odot)^4$ (Duric 2004). Therefore, the disc aspect ratio simplifies to:

$$h_{\mathrm{g,irr}} = 0.0245 \left(\frac{r}{1\,\mathrm{au}}\right)^{2/7} \tag{2.6}$$

independent of stellar mass.

If the inner disc is dominated by viscous heating, its temperature structure is highly related to the viscous accretion rate and opacity. Following Liu et al. (2019), s and q are taken to be $-3/8$ and $-1/16$, while $\Sigma_{1\mathrm{au}}$ and $h_{1\mathrm{au}}$ are not specified.

2.2.2 Type I migration

In the Type I migration regime, planet migration is the result of a net torque $\Gamma_{\rm net}$ consisting of the Lindblad (Ward 1986, 1997), corotation (Goldreich & Tremaine 1979; Ward 1992) and thermal torques (Benítez-Llambay et al. 2015; Masset 2017; Guilera et al. 2019, 2021), etc. Usually, the net torque is negative and the planet migrates inward. In the Type I limit the migration speed is proportional to disc mass and planet mass. In the limit of a locally isothermal disc, which implies that temperature is a function of radius only, $T(r)$, the type I migration time-scale for the i-th planet at distance r_i is:

$$\tau_{a_i} = \frac{L_i}{\Gamma_{\rm net}} = \frac{\gamma_I \tau_{w_i}}{h(r_i)^2}, \tag{2.7}$$

where L_i is the angular momentum of the planet, $\gamma_I = (2.7 - 1.1s)^{-1}$ (Tanaka et al. 2002) is the Type I migration prefactor (D'Angelo & Lubow 2010), and $h(r_i)$ is the disc gas aspect ratio at r_i. The characteristic time of the orbital evolution (Tanaka & Ward 2004) is:

$$\tau_{w_i} = \frac{1}{\mu_i} \frac{M_\star}{\Sigma(r_i) r_i^2} \frac{h(r_i)^4}{\Omega_K(r_i)}, \tag{2.8}$$

where μ_i is the mass ratio of the i-th planet over its host star and $\Omega_K(r_i) = \sqrt{GM_\star/r_i^3}$ is the Keplerian angular velocity at distance r_i. The eccentricity damping rate is proportional to the local surface density and planet mass. It is given by:

$$\tau_{e_i} = \frac{C_e \tau_{w_i}}{0.78} = \frac{C_e}{0.78\gamma_I} h^2 \tau_a, \tag{2.9}$$

where C_e stands for eccentricity damping efficiency. Although Cresswell & Nelson (2008) gives $C_e \approx 1$, lower values are needed in other studies to reproduce specific systems. TRAPPIST-1 planets demand $C_e \approx 0.1$ (Huang & Ormel 2022) and K2-24 requires $C_e \approx 0.28$ (Teyssandier & Libert 2020). A recently discovered ~100 Myr old exoplanet system TOI-1136, on the other hand, suggest $C_e \sim 10$ (Dai et al. 2022). We are therefore agnostic about the value of C_e, which value we intend to constrain through our MCMC fitting.

2.2.3 Dynamics of resonance trapping

Resonance trapping is a natural outcome of convergent disc migration and eccentricity damping, especially for first-order resonances $(j+1):j$. When two planets are in first-order resonance, their eccentricities and period ratio librate around their equilibrium values. Such equilibrium has been studied by Goldreich & Schlichting (2014) and Terquem & Papaloizou (2019). They both give the equilibrium eccentricity (the eccentricity where tidal damping equals resonant excitation) of the inner planet:

$$e^2_{1,\rm eq} = \frac{\tau_{e_1}/\tau_{a_2} - \tau_{e_1}/\tau_{a_1}}{2(j+1)\left(1 + \frac{j}{j+1}\frac{\mu_1}{\alpha\mu_2}\right)\left[1 + \frac{\mu_1}{\alpha\mu_2}\left(\frac{j}{j+1}\right)^2 \left(\frac{f_2'}{f1}\right)^2 \frac{\tau_{e_1}}{\tau_{e_2}}\right]} \tag{2.10}$$

where α is ratio of the inner-to-outer semi-major axis . Here, and in the following, the subscription '1' stands for the inner planet and '2' for the outer planet. The relationship between the eccentricities of the inner and outer planets is:

$$\frac{e_2^2}{e_1^2} = \left(\frac{\mu_1}{\alpha\mu_2}\frac{j}{j+1}\frac{f_2'}{f_1}\right)^2, \tag{2.11}$$

where f_1 and f_2' are coefficients tabulated in Terquem & Papaloizou (2019, their Table A1). The equilibrium value for the offset from exact resonance is:

$$\Delta_{\rm eq} = -f_2' \mu_1 \frac{1}{j} \frac{1}{e_{2,\rm eq}}. \tag{2.12}$$

At this distance, the resonance repulsion equals the Type-I inward migration.

In order to calculate the period ratios for planets in resonance, we need to know what their equilibrium eccentricities are. This calculation can be done only after the values of τ_{e_1}/τ_{e_2}, τ_{e_1}/τ_{a_2} and τ_{e_1}/τ_{a_1} are known. Combining the disc model and migration model, we have

$$\frac{\tau_{e_1}}{\tau_{e_2}} = \frac{\mu_2}{\mu_1} \left(\frac{r_1}{r_2}\right)^{4q-s-0.5} \tag{2.13}$$

and

$$\frac{\tau_{e_1}}{\tau_{a_2}} = \frac{\tau_{e_2}}{\tau_{a_2}} \frac{\tau_{e_1}}{\tau_{e_2}} = \frac{C_e h(r_2)^2}{0.78\gamma_I} \frac{\mu_2}{\mu_1} \left(\frac{r_1}{r_2}\right)^{4q-s-0.5} \tag{2.14}$$

where s and q are gas surface density and aspect ratio gradient.

For the eccentricity-to-semi-major axis damping of the inner planet, we distinguish it between two cases:

1. `Migrating` pair. If resonances are formed during migration and the ambient disc disperses before the planet pairs reach a migration barrier, planet migration and eccentricity damping follow Eq. (2.7) and Eq. (2.9). Therefore,

   $$\frac{\tau_{e_1}}{\tau_{a_1}} = \frac{C_e h(r_1)^2}{0.78\gamma_I} \tag{2.15}$$

   It requires that the outer planet migrates faster than the inner planet to guarantee convergent migration.

2. `Braking` pair. On the other hand, if resonances are formed before/after the inner planet's migration is halted by a barrier (could be disc inner edge or the radius where reverse migration occurs), there is no net torque on the two planets. Angular momentum conservation gives $\tau_{a_1}/\tau_{a_2} = -\sqrt{\mu_1 r_1/\mu_2 r_2}$. Hence,

   $$\begin{aligned} \frac{\tau_{e_1}}{\tau_{a_1}} &= -\frac{C_e h(r_2)^2}{0.78\gamma_I} \left(\frac{\mu_2}{\mu_1}\right)^{\frac{3}{2}} \left(\frac{r_1}{r_2}\right)^{4q-s-1} \\ &= -\frac{C_e h(r_1)^2}{0.78\gamma_I} \left(\frac{\mu_2}{\mu_1}\right)^{\frac{3}{2}} \left(\frac{r_1}{r_2}\right)^{2q-s-1} \end{aligned} \tag{2.16}$$

For the outer planet $\tau_{e_2}/\tau_{a_2} = C_e h(r_2)^2/0.78\gamma_I$ is always true. It is also apparent that the resonant equilibrium does not depend on disc mass ($\Sigma_{1\rm au}$) but on power law indices and aspect ratio (s, q, and $h_{1\rm au}$).

2.2.4 Mass-radius relations

Planets' masses are also needed to calculate the equilibrium period ratios in resonance. However, most transiting planets have poorly constrained masses compared to their radii.

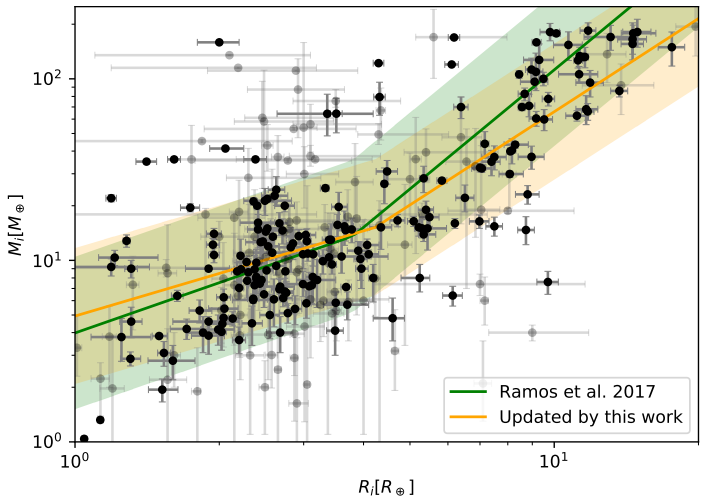

Figure 2.1. Mass-radius (M-R) relationship for exoplanets. Planets are selected based on the data of transiting planets in the NASA Exoplanet Archive. Only planets with mass lower than $200M_\oplus$, radii smaller than $20R_\oplus$ and periods longer than 5 days are included in the sample. Planets' masses and radii are indicated by black dots, with 1σ error bars. The green colour indicates the fit result from Ramos et al. (2017), orange colour is the updated fit result by this work (Eq. (2.17)). The values within their 1σ dispersion ($\sigma_\mathrm{m} = 0.374$ for our fit) are contained within the light green and orange region respectively.

If the planet mass is not yet constrained from e.g., Transit Timing Variation (TTV Agol et al. 2005) or Radial Velocity (RV), we then obtain the planet mass using a mass-radius relation. The planet sample for fitting the mass-radius relation is based on the data of transiting planets from the NASA Exoplanet Archive[1]. Planets with masses lower than $200M_\oplus$, radii smaller than $20R_\oplus$, or periods longer than 5 days (see Sect. 2.4.1) are selected while planets with periods shorter than 5 days are excluded.

Our fitting approach is identical to Ramos et al. (2017). They use a broken power law expression, which fits two different power law relations for larger bodies ($R > R_\mathrm{crit}$) and smaller bodies ($R < R_\mathrm{crit}$).

$$\log_{10}\left(\frac{\overline{M_i}}{M_\oplus}\right) = \begin{cases} a + b\log_{10}\left(\frac{R_i}{R_\oplus}\right) & \text{if } R_i \leq R_\mathrm{crit} \\ c + d\log_{10}\left(\frac{R_i}{R_\oplus}\right) & \text{if } R_i > R_\mathrm{crit} \end{cases} \tag{2.17}$$

where M_i and R_i is the mass and radius of the i-th planet. We make use of the Maximum Likelihood Estimator (MLE) to maximize a Gaussian likelihood centered at Eq. (2.17). The critical radius R_crit is also fitted. It estimates that: $a = 0.69$, $b = 0.78$, $c = 0.11$, $d = 1.7$, $R_\mathrm{crit} = 4.23R_\oplus$ and the corresponding dispersion $\sigma_m = 0.374$. The best-fitting relation is shown in Fig. 2.1 in comparison with the relation fitted by Ramos et al. (2017). They do not differ significantly. The estimated value for R_crit is consistent with Teske et al. (2021) who suggest a single power law relation for planets with $R < 3.25R_\oplus$.

Equation (2.17) allows us to calculate the planet mass and therefore the resonance offset (Eq. (2.12)). Moreover, the log-normal dispersion in planet mass enables us to check our model consistency. The reason is that any uncertainty in the mass, will propagate, through

[1] `https://exoplanetarchive.ipac.caltech.edu`

Eq. (2.10) and Eq. (2.12). Therefore, we expect that the obtained value for σ_Δ from MCMC fitting is similar to, or exceeds, σ_m.

The log-normal dispersion in planet mass significantly simplifies our analysis. There are arguably more sophisticated forms of M-R relationships, e.g., the one given by Wolfgang et al. (2016) and improved by Teske et al. (2021). However, they assume planet mass follows a normal dispersion instead of a log-normal. In that case, the resulting Δ would follow a complicated form of the ratio distribution[2].

2.2.5 A statistical model of resonant and non-resonant planets

We define the posterior distribution as: $p(\boldsymbol{\theta}|\Delta_{\mathrm{obs},k}, \boldsymbol{X}_k) = p(\Delta_{\mathrm{obs},k}|\boldsymbol{\theta}, \boldsymbol{X}_k)p(\boldsymbol{\theta}|\boldsymbol{X}_{\mathrm{obs},k})$. If the disc structure is not specified (without knowing the specific values of s, q in Eq. (2.2) and Eq. (2.3)), the unknown model parameters are $\boldsymbol{\theta} = (\log_{10}(C_e h_{1\mathrm{au}}^2), \sigma_\Delta, s, q)$ and the known parameters $\boldsymbol{X}_k = (M_\star, M_1, M_2, r_1, r_2, j)$. The index k indicates the k-th planet pair. If a disc structure is specified, the unknown model parameters are $\boldsymbol{\theta} = (\log_{10} C_e, \sigma_\Delta)$ for the irradiation disc and $\boldsymbol{\theta} = (\log_{10}(C_e h_{1\mathrm{au}}^2), \sigma_\Delta)$ for the viscous disc, and the known parameters are $\boldsymbol{X}_k = (M_\star, M_1, M_2, r_1, r_2, j, h_{1\mathrm{au}}, s, q)$. We assume that the prior $p(\boldsymbol{\theta}|\boldsymbol{X}_k)$ follows a uniform distribution (Table 2.1). The resonance index j is regarded as one of the known parameters such that we can analyse all pairs at once.

As mentioned, resonance trapping naturally results from convergent migration: either two planets get trapped into resonance during migration (both inward) with the outer planet migrating faster than the inner one, or the inner planet reaches a migration barrier with the outer planet arriving at a later time. Following the discussion in Sect. 2.2.4, we assume that the period ratio of a planet pair that is in resonance obeys a log-normal distribution $\log_{10}\Delta \sim \mathcal{N}(\log_{10}\Delta_{\mathrm{m/s}}(\boldsymbol{\theta}, \boldsymbol{X}_k), \sigma_\Delta^2)$:

$$
\begin{aligned}
&p_{\mathrm{res,m/s}}(\Delta|\boldsymbol{\theta}, \boldsymbol{X}_k) d\log_{10}\Delta \\
&= \frac{1}{\sqrt{2\pi\sigma_\Delta^2}} \exp\left[-\frac{[\log_{10}\Delta - \log_{10}\Delta_{\mathrm{m/s}}(\boldsymbol{\theta}, \boldsymbol{X}_k)]^2}{2\sigma_\Delta^2}\right] d\log_{10}\Delta,
\end{aligned}
\tag{2.18}
$$

where $\Delta_{\mathrm{m/s}}$ indicates the resonance commensurability calculated by Eq. (2.12). The resonance offset Δ_{m} indicates the value calculated for `Migrating` pairs using Eq. (2.15), while Δ_{s} is for `Braking` pairs and is calculated using Eq. (2.16).

In the Type I migration regime, if the inner planet is more massive (migrates faster), convergent migration can only occur when the inner planet has reached the migration barrier. On the other hand, if the inner planet's migration is slower than the outer, migration is always convergent. In that case, trapping can occur when both planets migrate inward or when the inner planet has reached the migration barrier. For ease of the likelihood calculation, we further divide the resonant planet pairs into three categories:

Group 1: The inner planet migrated slower ($\tau_{a_1} > \tau_{a_2}$) and it did not reach a migration barrier (N_1);

Group 2: The inner planet migrated slower ($\tau_{a_1} > \tau_{a_2}$) and it reached a migration barrier (N_2);

Group 3: The inner planets migrated faster ($\tau_{a_1} \leq \tau_{a_2}$) and it reached a migration barrier (N_3).

[2] If variables X and Y follow a dependent (independent) normal distribution with nonzero mean values, the new variable $Z = X/Y$ follows correlated (uncorrelated) non-central normal ratio distribution (Hinkley 1969; Hayya et al. 1975).

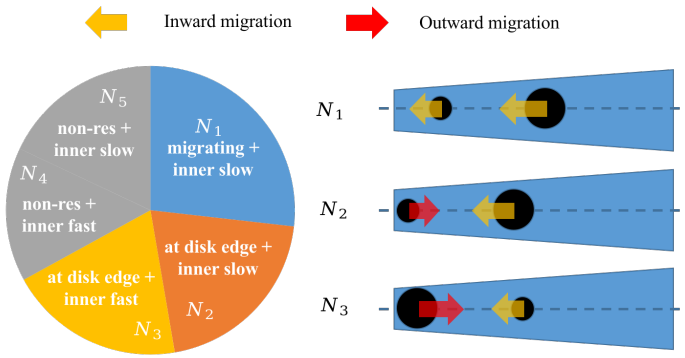

Figure 2.2. Classification of resonant and non-resonant planet pairs. In the pie chart, 'migrating' means the pairs lock into resonance before reaching a migration barrier, whereas "at disc edge" indicates planets lock into resonance at a planet migration trap. "Inner slow" ("fast") means that the inner planet has a longer (shorter) migration time-scale than its outer planet. $N_{\rm res}$ is the number of resonant pairs. N_1, N_2, and N_5 are the numbers of `Migrating`, `Braking`, and non- resonant pairs in the pairs with the inner planets migrating slower than the outer. N_3 and N_4 are the numbers of `Braking` and non-resonant pairs among the pairs with inner planets migrating faster than the outer.

N_1, N_2 and N_3 represent the number of resonant planet pairs corresponding to each type of resonance. In addition, N_4 (N_5) represents the number of pairs that are not in resonance with the inner planet migrating faster (slower) than the outer planet. We provide a sketch to explain the five classes in Fig. 2.2.

If the inner planets migrate faster ($\tau_{a_1} \leq \tau_{a_2}$), those pairs in resonance must be `Braking` pairs. However, if the inner planets migrate slower, they could either be `Migrating` pairs or `Braking` pairs. The $\log_{10}\Delta$ distribution of planets in resonance is therefore (hereafter, $p_{\rm res}(\Delta)$ represents $p_{\rm res}(\Delta_{\rm obs}|\boldsymbol{\theta}, \boldsymbol{X}_k)$, etc):

$$p_{\rm res}(\Delta) = \begin{cases} p_{\rm res,s}(\Delta) & \text{if } \tau_{a_1} \leq \tau_{a_2}, \\ \left[p_{\rm res,s}(\Delta) + p_{\rm res,m}(\Delta)\right] & \text{if } \tau_{a_1} > \tau_{a_2}. \end{cases} \tag{2.19}$$

The period ratio of planet pairs that are not in resonance is assumed to follow a uniform distribution:

$$p_{\rm n-res}(\Delta) d\log_{10}\Delta = \frac{(\ln 10)\Delta}{\Delta_{\rm max}} d\log_{10}\Delta \tag{2.20}$$

where $\Delta_{\rm max}$ is the value above which a planet pair with $\Delta_{\rm obs}$ is not considered in resonance. We use $\Delta_{\rm max} = (3j+2)/(3j-1) - (j+1)/j$ which is the distance from the first order $(j+1):j$ resonance to its closest external 3rd order $(3j+2):(3j-1)$ resonance.

Finally, the total log-likelihood is written as:

$$\ln\mathcal{L} = \sum_{k=1}^{N_{\rm pairs}} \ln\left[p_{\rm res}(\Delta_{{\rm obs},k}) + p_{\rm n-res}(\Delta_{{\rm obs},k})\right], \tag{2.21}$$

where $N_{\rm pairs}$ is the number of planet pairs in our sample.

Parameter	Prior		
	General	Irradiation	Viscous
$\log_{10}(C_e h_{1\mathrm{au}}^2)$	$\mathcal{U}(-8,0)$	–	$\mathcal{U}(-8,0)$
$\log_{10} C_e$	–	$\mathcal{U}(-2,2)$	–
σ_Δ	$\mathcal{U}(0,1)$	$\mathcal{U}(0,1)$	$\mathcal{U}(0,1)$
s	$\mathcal{U}(-5,2.4)$	$-15/14$	$-3/8$
q	$\mathcal{U}(-2,2)$	$2/7$	$-1/16$
$h_{1\mathrm{au}}$	–	0.0245	–

Table 2.1. Prior bounds or values for the disc parameters of the three models. All priors follow a uniform distribution $\mathcal{U}$.

2.3 Resonance Trapping criterion for the restricted 3-body problem

In this section, we improve and numerically verify the two-body resonance trapping criterion. This new trapping condition will be used in Sect. 2.5.2 to further constrain the statistical results of Sect. 2.4.2.[3]

2.3.1 Theoretical Derivation

In the restricted three-body problem, the outer planet is on a fixed circular orbit. The inner planet moves outward and its semi-major axis and eccentricity are damped on time-scales of τ_a and τ_e, respectively. Lagrange's planetary equation for the mean motion (n) then reads:

$$\dot{n}_1 = -3j\alpha f_1 \mu_2 e_1 n_1^2 \sin\phi_1 - \frac{3n_1}{2\tau_a} + \frac{p e_1^2 n_1}{\tau_e}, \tag{2.22}$$

where $\alpha = a_1/a_2$, ϕ_1, e_1 and f_1 are the semi-major axis ratio, resonance angle, the eccentricity of the inner planet, and f_1 is a numerical factor that depends on the resonance index j (Murray & Dermott 1999; Terquem & Papaloizou 2019). By definition, $p = 3$ holds when the eccentricity damping operates at constant angular momentum (Teyssandier & Terquem 2014). Lagrange's planetary equation for eccentricity is:

$$\dot{e}_1 = -\alpha f_1 \mu_2 n_1 \sin\phi_1 - \frac{e_1}{\tau_{e_1}}, \tag{2.23}$$

When two planets are in resonance, the values of different orbital properties e.g., e_1, α and ϕ_1 librate around their equilibrium values. The equilibrium eccentricity (Goldreich & Schlichting 2014; Terquem & Papaloizou 2019) is derived by putting $\dot{e} = \dot{a} = 0$ and eliminating $\sin\phi_1$ in Eq. (2.22) and Eq. (2.23):

$$e_{1,\mathrm{eq}} = \sqrt{\frac{\tau_{e_1}}{2(j+1)\tau_{a_1}}}. \tag{2.24}$$

By inserting the equilibrium eccentricity $e_{1,\mathrm{eq}}$ and $\alpha_{\mathrm{eq}} \approx [j/(j+1)]^{2/3}$ into Eq. (2.23), $\sin\phi_1$ follows:

$$\sin\phi_{1,\mathrm{eq}} = -\frac{1}{\alpha f_1 \mu_2 n_1}\sqrt{\frac{1}{2(j+1)\tau_{e_1}\tau_{a_1}}} \tag{2.25}$$

[3] Batygin & Petit (2023b) have recently presented an analysis with a trapping condition also predicated on the equilibrium phase angle, Eq. (2.25), like in this Section. Their findings are consistent with ours.

Naturally, its absolute value cannot exceed 1. Otherwise, for $|\sin\phi_1| > 1$, no steady state exists and the planets will cross the resonance. Combining, $\dot{e}_1 = 0$, Eq. (2.23) and Eq. (2.24) we can write the resonance trapping condition:

$$\tau_{a_1}\tau_{e_1} \geq \frac{1}{2(j+1)(\alpha f_1 \mu_2 n_1)^2}. \tag{2.26}$$

The classical theory about the resonance trapping criterion is that the time for the planet to migrate across the libration width is shorter than the libration time-scale (Ogihara & Kobayashi 2013; Batygin 2015). For comparison, we also provide the criterion derived from the classical pendulum model (Murray & Dermott 1999; Ogihara & Kobayashi 2013; Huang & Ormel 2022):

$$\tau_{a_1}\tau_{e_1} \geq \frac{\pi(j+1)}{4(\alpha f_1 \mu_2 n_1)^2}. \tag{2.27}$$

Compared to Eq. (2.27), the new criterion (Eq. (2.26)) has the same dependence on planet-to-star mass ratio μ_2 and the orbital frequency n_1 but differs regarding the resonance index j.

2.3.2 Comparison with simulation

We compare the new resonance trapping criterion above against the numerical simulation. The fiducial accelerations accounting for migration and eccentricity of planets in the simulations are expressed by:

$$\boldsymbol{a}_{\rm m} = -\frac{\boldsymbol{v}}{2\tau_a}, \tag{2.28}$$

$$\boldsymbol{a}_{\rm e} = -2\frac{(\boldsymbol{v}\cdot\boldsymbol{r})\boldsymbol{r}}{2r^2\tau_e} \tag{2.29}$$

(Papaloizou & Larwood 2000; Cresswell & Nelson 2006, 2008). We make use of the `WHfast` integrator of the open-source N-body code REBOUND (Rein 2012). The migration and eccentricity damping on planets are implemented through REBOUNDx (Tamayo et al. 2020).

We fix the outer planet on a circular orbit at $[(j+1)/j]^{2/3}$ au. The inner planet starts to migrate outward at 0.8 au on a time-scale of τ_a. Its eccentricity is damped on a time-scale of τ_e. The planet mass is fixed at $10\,M_\oplus$ and the host mass is $1\,M_\odot$. We vary two parameters in the simulation: τ_a from 10^4 yr (fast migration) to 10^7 yr (slow migration), and τ_a/τ_e ranging from 10^1 (inefficient eccentricity damping) to 10^4 (efficient eccentricity damping). Each parameter is sampled by 100 grid points evenly distributed in log-space. In order to capture the probabilistic behavior of resonance trapping, we run five simulations for each point in the τ_a/τ_e–τ_a parameter space, where we evenly sample the initial longitude of the inner planet.

We conduct simulations for $j = 1$ (2:1 resonance) and $j = 2$ (3:2 resonance). We run the simulation until $t = \tau_a$, but we take a snapshot at $t = 0.2\tau_a$. If the period ratio P_2/P_1 decreases below $(j+1)/j$, we classify the simulation outcome as a resonance crossing. The results are shown in Fig. 2.3 and Fig. 2.4 for $j = 1$ and $j = 2$ respectively. Resonance crossing cases are in white and resonance trapping cases are in green. The red dashed line indicates the boundary below which the trapping solution becomes overstable,

$$\left(\frac{\tau_a}{\tau_e}\right)_{\rm overstable} = \frac{1}{8(j+1)}\left(-\frac{3j^2}{\alpha f_1 \mu_2}\right)^{2/3} \tag{2.30}$$

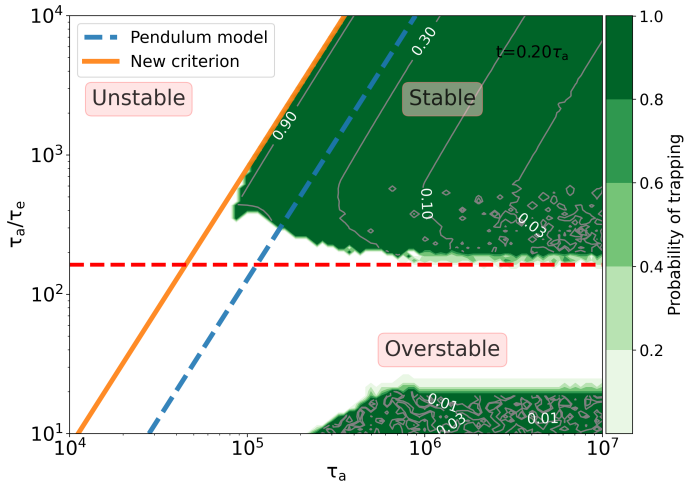

Figure 2.3. Resonance trapping and crossing for the 2:1 resonance. For each point in the parameter space, we run five simulations with different initial conditions to obtain the probabilistic result of resonance trapping (green shading). The blue line is the resonance trapping criterion derived from the pendulum model (Eq. (2.27)) while the orange line is our newly derived criterion (Eq. (2.26)). The grey solid lines are the contours of $\sin\phi_1$, with corresponding values labelled in white. The red dashed line (Eq. (2.30)) corresponds to the transition from stable resonance trapping (above) to overstable resonance (below). Below this line, the simulations progressively evolve into the overstable territory, see `https://raw.githubusercontent.com/shuohuangGIT/Infer-migration-history/main/q1.mp4`.

(Goldreich & Schlichting 2014), which evaluates to $\tau_a/\tau_e \approx 170$ for $\mu_2 = 3\times10^{-5}$, both for $j = 1$ and 2. Above this line, all systems are either trapped in resonance or not. The top-right corner indicates the parameter space where the two planets both get captured and permanently stay in resonance and the top-left indicates resonance crossing. Below this line, some systems are still evolving and resonance trapping is only temporary.

We indicate the trapping criterion derived from the pendulum model in blue and the improved trapping criterion (Eq. (2.26)) with the orange line. From Fig. 2.3 and 2.4 it is clear that the pendulum model criterion for resonance trapping (blue line) fails to quantitatively match the numerical simulations. Our new criterion (orange line), however, fits the simulations perfectly. The equilibrium value of $\sin\phi_1$ for the simulation snapshots is calculated by averaging its value over a time span of $0.1\tau_a$ before and after the snapshot time, e.g., $0.1-0.3\tau_a$ for the snapshot at $t = 0.2\tau_a$. The values of $\sin\phi_{1,\rm eq}$ is indicated by grey solid lines (contour) in Fig. 2.3 and 2.4. $\sin\phi_{1,\rm eq}$ increases as getting closer to the orange line, which is also expected by Eq. (2.25). The picture of resonance trapping/crossing over the entire parameter space of the migration time-scale and eccentricity damping time-scale has now been clarified. Migration plays a role in exciting the planet's eccentricity, while eccentricity damping reduces it. On one hand, if a planet pair is in resonance, the eccentricity damping balances its excitation and finally librates near the equilibrium value. If the migration speed is so fast that there is no steady state solution for the resonance angle $\phi_{1,\rm eq}$ (Eq. (2.26)), the resonance is crossed. Otherwise, resonance trapping is ensured. On the other hand, if eccentricity is excited to be high enough, planets can be captured into resonance, but only temporarily, because of the continuous increase of the resonance libration amplitude (over-

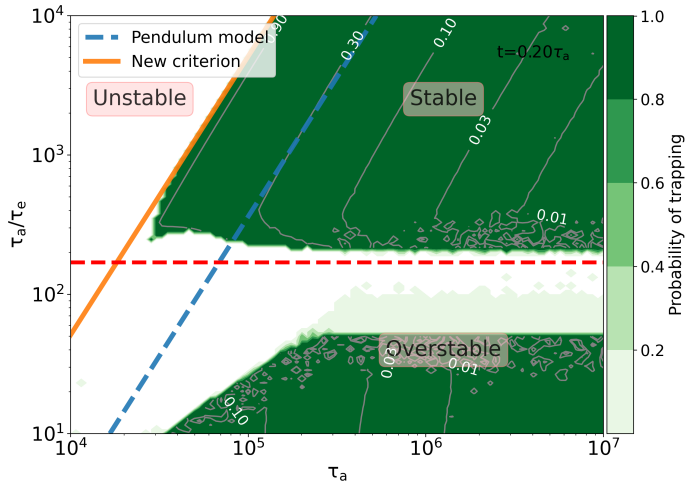

Figure 2.4. Same as Fig. 2.3, but for the 3:2 resonance. The video can be downloaded on Github: `https://raw.githubusercontent.com/shuohuangGIT/Infer-migration-history/main/q2.mp4`.

stability, cf. Goldreich & Schlichting 2014). Although not evident from the figures presented, all simulations located in the large green corner above the red dashed line exhibit permanent libration of $\sin\phi_1$, indicating that the planets are captured in resonance permanently. The amplitude of $\sin\phi_1$ during libration increases as the ratio τ_a/τ_e decreases, and approaches the red dashed line denoting overstability in Fig. 2.3 and 2.4. The green region situated below the red dashed line represents simulations in which planets are temporarily captured in resonance, with their amplitude of $\sin\phi_1$ increasing over time and circulating at the end of the simulation. In conclusion, both efficient eccentricity damping (τ_a/τ_e is high) and slow migration are required for permanent resonance trapping.

2.4 MCMC analysis

In this section, we first discuss how we select our sample in Sect. 2.4.1. Then we conduct an MCMC fitting to constrain the model parameters.

2.4.1 Sample selection

Our sample selection and all analysis are based on the NASA Exoplanet Archive. Our attention is drawn to planets detected through transits and TTV. As shown in Sect. 2.2.3, we need planets' masses to calculate the equilibrium eccentricities and period ratios in resonance. If only the radius is available, the M-R relationship described in Sect. 2.2.4 is used to calculate the masses of those transiting planets. Additionally, the semi-major axes and stellar masses are extracted.

We do not consider short-period planets in our sample. We take this simple step to reduce the effects of both photo-evaporation and stellar tides on the M-R relationship. First, photo-evaporation can alter the M-R relationship for planets with low-density atmospheres on time-scale of 1 Gyr (Fulton & Petigura 2018). It is believed to have triggered the so-called

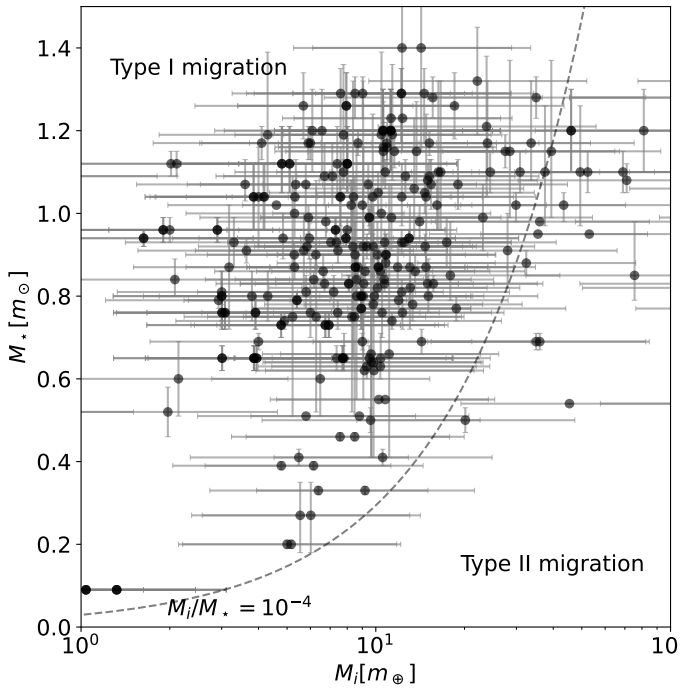

Figure 2.5. Planet mass versus stellar mass in the sample. Planet pairs with period ratios larger than $(j+1)/j$ and smaller than $(3j+2)/(3j-1)$ are chosen. We take j equal to 1, 2, 3 and 4. Planet masses and their host masses are indicated by black dots, with 1σ error bar. If the planet mass is inferred from its radius through the M-R relation, its uncertainty of the masses is assigned to be $\sigma_{\rm m} = 0.374$ dex. The grey dashed line indicates the position where the planet-to-star mass ratio equals $\mu = 10^{-4}$. We assume planets to the left of this line to follow Type I migration and otherwise Type II. Only Type I migrating planets are included in our analysis.

'radius gap' (Fulton et al. 2017). When planets get closer to their host stars, this effect is more obvious (Fulton & Petigura 2018). Second, stellar tides alter close-in planets' orbital properties (Lithwick & Wu 2012; Batygin & Morbidelli 2013; Charalambous et al. 2018; Papaloizou et al. 2018) and blur the information of the planets inherited from their protoplanet disc. Both mechanism are very sensitive to planets' semi-major axes. Excluding the planets with a cutoff period shorter than 5 days, though crude, can suppress the interference from stellar tides (Choksi & Chiang 2020) and photo-evaporation (Fulton & Petigura 2018) on our sample.

We display the planet mass versus their host mass in Fig. 2.5. The average planet mass is $10M_\oplus$ and the average stellar mass is $1\,M_\odot$. The planets' and stars' mass uncertainties are indicated by error bars. If the planet mass is inferred from the M-R relation, the log-normal standard deviation is then $\sigma_m = 0.374$ (Eq. (2.17)). The migration speed of low-mass planets in the proto-planetary disc scales linearly with planet mass, as dictated by the Type I migration limit. As planets become massive enough to perturb their surrounding disc, their migration gradually switches to Type II (Kanagawa et al. 2018; Pichierri et al. 2022). We set the boundary between two types of migration as $\mu_{\rm trans} = 10^{-4}$. Since our interests focus on Type I migration only planets with $\mu < \mu_{\rm trans}$ are included in our sample.

Finally, the sample size is reduced to 371 and the period ratios for all planet pairs are given

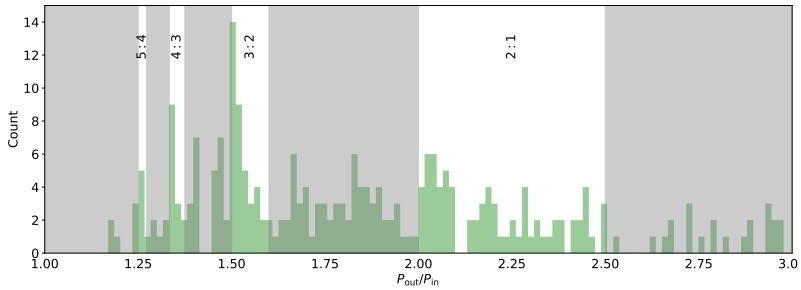

Figure 2.6. Distribution of the period ratio of all observed planet pairs in our sample (green histograms). We highlight the four windows in the vicinity of four different first-order resonances: 2:1, 3:2, 4:3 and 5:4. The left boundary of each window is $(j+1)/j$ and the right boundary is $(3j+2)/(3j-1)$. The total number of pairs is 371 in the green histogram and 128 in the windows.

by Fig. 2.6. The selected planets come from systems with two and more planets, including those with resonance chains.

To calculate the resonance offset, the resonance number j is required. There are excesses of systems ('peaks') just wide of the integer period ratios, which is suggestive of resonances. We only consider first-order resonances: 2:1, 3:2, 4:3, and 5:4. We assume that planets with period ratios slightly larger than the integer ratios are potentially in resonance until the period ratio "hits" the third-order resonance, because the resonant interaction is weaker as they become further from exact commensurability. Planet pairs with period ratios larger than $(j+1)/j$ but smaller than $(3j+2)/(3j-1)$ are possibly in $(j+1)/j$ resonance. Here, $(3j+2)/(3j-1)$ is the location of the closest third-order resonance. The selection of a period ratio limit for identifying planets in 2:1 resonance may seem arbitrary, given that the period ratio can extend up to 2.5, where planet pairs are unlikely to be in resonance. However, a slightly smaller window for the 2:1 resonance would not affect our conclusions. Nonetheless, this choice is useful for identifying planets in 3:2, 4:3, and higher j first-order resonances because planets located near these resonance locations are close to nearby higher-order resonances, and may therefore be more easily perturbed. The satisfied period ratio windows are highlighted in Fig. 2.10 (top panel) and the four lower panels zoom in on these four windows, for j =1, 2, 3, 4, where we instead show the distribution of the offset from resonance, Δ. Planets out of the windows may still be in first-order resonance, but their fraction must be very low and it is not covered by our analysis. We ignore other first-order resonances and all higher-order resonances.

2.4.2 Implication on planet-disc interaction from MCMC

We use `emcee` (Foreman-Mackey et al. 2013) to perform the MCMC analysis. We implement three different models:

1. General model. The disc structure is not specified and the MCMC is used to fit $\log_{10}(C_e h_{1au}^2)$, σ_Δ, s, q.

2. Irradiation model. Stellar irradiation is assumed to be the main heating source and the MCMC is used to fit $\log_{10} C_e$ and σ_Δ.

3. Viscous model. Viscosity-driven accretion is assumed to be the main heating source and the MCMC is used to fit $\log_{10}(C_e h_{1au}^2)$, σ_Δ.

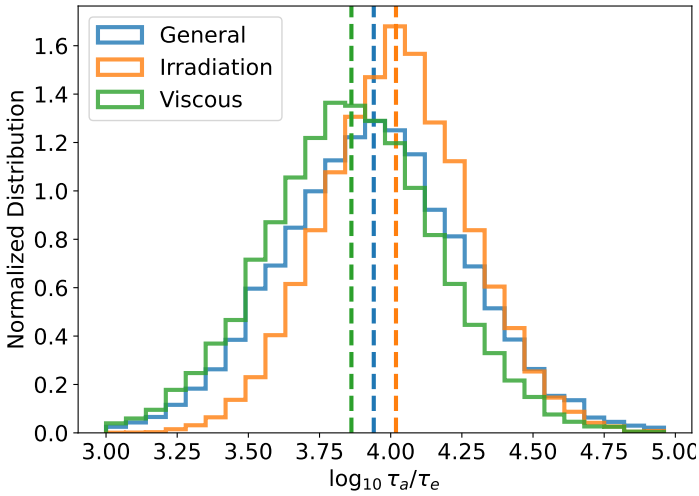

Figure 2.7. Distribution of $\log_{10}\tau_a/\tau_e$, the semi-major axis-to-eccentricity damping time-scale at the location of the inner planets averaged over all planet pairs, in General (blue), Irradiation (orange) and Viscous (green) model. We calculate this quantity based on the posterior distributions of the parameters in each model. Dashed lines indicate their median values.

The prior distribution of parameters $\log_{10}(C_e h_{1\mathrm{au}}^2)$, $\log_{10} C_e$, σ_Δ, s, q and the values we take for s, q and $h_{1\mathrm{au}}$ for the three different models are shown in Table 2.1. The convergence of MCMC chains are checked. We make use of the criterion that MCMC converges if the autocorrection time is shorter than 1/50 times its chain length. We checked that our results all satisfied the convergence criterion.

For the General model, we examine whether our method is capable to retrieve all the parameters in Appendix 2.B. It turns out that almost all parameters are degenerate. Therefore, the fitted values for $\{\log_{10}(C_e h_{1\mathrm{au}}^2), \sigma_\Delta, s, q\}$ may not be reliable (Appendix 2.B.1). The result of the General model is shown and analysed in Appendix 2.A. We also calculate the quantity $\log_{10}\tau_a/\tau_e$, the semi-major axis-to-eccentricity damping time-scale, at the location of the inner planets averaged over all planet pairs. This quantity, however, shows to be independent of the other parameters and can be reproduced within the 1σ error bar (Appendix 2.B.1).

We calculate $\log_{10}\tau_a/\tau_e$ in all three models, and their distributions are shown in Fig. 2.7. Two key points can be made. First, different disc structures result in nearly identical distributions. The parameter $\log_{10}\tau_a/\tau_e$ is not sensitive to the assumed disc structure. Second, the value of $\log_{10}\tau_a/\tau_e$ – peaking at 4 and almost always larger than 3 – is high. The high semi-major axis-to-eccentricity damping time-scale ratio indicates that temporary capture (overstable libration) did not operate for the planets in our sample, which would require $\tau_a/\tau_e \approx 170$ (Goldreich & Schlichting 2014) in Eq. (2.30).

By specifying the disc structure – the Irradiation or Viscous model – the parameters can be successfully retrieved within 1σ error bar (Appendix 2.B.2). We show the fit result of $\{\log_{10} C_e,\ \sigma_\Delta\}$ and $\{\log_{10}(C_e h_{1\mathrm{au}}^2),\ \sigma_\Delta\}$ for the Irradiation and Viscous model in Fig. 2.8 and Fig. 2.9, respectively. The python package `corner.py` (Foreman-Mackey 2016) is used to generate the plots of the posterior distributions.

The Irradiation model (Fig. 2.8) fits $\log_{10} C_e = 0.94^{+0.25}_{-0.25}$. For the viscous model, the disc aspect ratio is sensitive to the stellar accretion rate and disc opacity. Therefore, we fit the combination $C_e h_{1\mathrm{au}}^2$, and $\log_{10}(C_e h_{1\mathrm{au}}^2) = -4.60^{+0.30}_{-0.29}$ (Fig. 2.9). If we take $h_{1\mathrm{au}} = 0.0245$,

same value as the irradiation model, then $\log_{10} C_e = -1.38^{+0.30}_{-0.29}$. Increasing $h_{1\mathrm{au}}$ (or $L_\star$ in Eq. (2.5)) would result in a smaller value of C_e ($C_e \propto h_{1\mathrm{au}}^{-2}$). Theoretically, Tanaka et al. (2002) and Tanaka & Ward (2004) from the first principle calculate that $\log_{10} C_e = 0$ for locally isothermal discs. The fitting outcomes from both disk models suggest more efficient eccentricity damping than theories.

Additionally, the fitted values for σ_Δ are $0.65^{+0.10}_{-0.08}$ and $0.79^{+0.10}_{0.09}$ for the Irradiation and Viscous model, respectively. Their values are twice that of the mass dispersion. Indeed, we expect that the fitted σ_Δ is of the same magnitude as σ_m (Sect. 2.2.4). However, σ_Δ is fitted to be slightly larger than our expectation. This could be an implication of turbulent discs (Rein & Papaloizou 2009; Goldberg & Batygin 2022) and/or post-disc perturbations (e.g. Lithwick & Wu 2012; Chatterjee & Tan 2014; Stock et al. 2020). We further run an MCMC fitting fixing σ_Δ to 0.374, the resulting posterior distribution of $\log_{10} C_e$ or $\log_{10}(C_e h_{1\mathrm{au}}^2)$ are not significantly different from what we present here. It gives $\log_{10}(C_e h_{1\mathrm{au}}^2) = -3.95^{+0.29}_{-0.27}$ for the Viscous model and $\log_{10} C_e = 0.44^{+0.19}_{-0.20}$ for the Irradiation model.

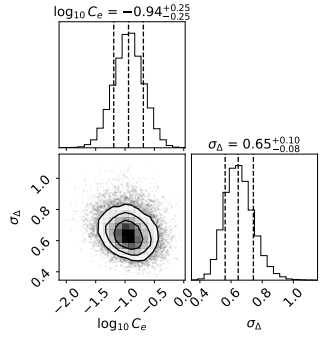

Figure 2.8. Corner plot of variables in the MCMC analysis ($\log_{10} C_e$ and σ_Δ) with 1σ, 2σ and 3σ confidence contours, for the Irradiation model, which fixes the surface density power law index $s = -15/14$ and the disc aspect ratio index $q = 2/7$. The 1σ uncertainty is labelled on the top of each column and indicated by left and right dashed lines. The middle dashed lines indicate their median values.

In summary, our MCMC model shows that eccentricity damping is effective ($\log_{10} \tau_a/\tau_e \approx 4$), making resonant over-stability unlikely. The observed period ratio excess of planets suggests more efficient eccentricity damping than the predictions by Tanaka et al. (2002) and Tanaka & Ward (2004) ($C_e \approx 1$), irrespective of whether the disk structure is dominated by irradiation or viscous heating. However, the aspect ratio of a viscous inner disc depends on the disc opacity and stellar accretion rate (e.g. Liu et al. 2019), which limits our ability to constrain C_e.

2.5 Implications for planet formation

In this section, we adopt the fit result from the Irradiation model and further study the implications of resulting resonant planets statistically. Ramos et al. (2017) and Charalambous et al. (2022) use similar prescription for their disc structure. The reason why we choose the Irradiation model is the following. Even though resonance trapping can happen much earlier, planets' period ratios (offsets) are more evolved at the end of the disc lifetime when the migration and eccentricity damping time-scales are longer than the disc dispersal time-scale.

The disc structure at this stage mostly determines what the corresponding mature planet system looks like. Because planet formation consumes solids and solids drift inward rapidly due to gas drag (Weidenschilling 1977; Andrews et al. 2012), the disc at this point becomes optically thin, rendering stellar irradiation the main heating source. The transition disc LkCa15 is arguably an example that low-mass planets can carve a large dust cavity (Leemker et al. 2022). Therefore, the Irradiation model is more applicable to transition discs.

The best-fitting resonance offset distribution is plotted in Fig. 2.10 (blue lines), with upper and lower 3σ uncertainty (blue shaded regions). We assume that the offset of non-resonant pairs follows a uniform distribution, which is also indicated in Fig. 2.10 (grey dashed lines). The MCMC fits the observed distribution better than the uniform-only model because it fits more planets with small Δ and fewer planets with large Δ, just as observed. The complete sample with 128 pairs are fitted simultaneously. However, we use four panels to display the four near-resonance planets because Δ depends on the resonance number j in a complex form. We cannot present one distribution of Δ to represent all 128 pairs while keeping the shape of log-normal profile.

For each planet pair, we calculate its probability of being in resonance ($P_{\mathrm{res},k}$, in Sect. 2.5.1). The total number of resonant pairs and planets' mean eccentricities in our sample is then obtained. The properties of their birthplace – the natal proto-planet disc – are then inferred, e.g., the upper limit of the surface density (Sect. 2.5.2) and the location of the migration barrier (Sect. 2.5.3).

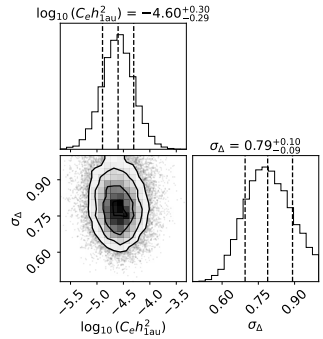

Figure 2.9. Similar to Fig. 2.8, but for the Viscous model. The surface density power law index is fixed at $s = -3/8$ and the disc aspect ratio index at $q = -1/16$.

2.5.1 Fraction of resonant pairs

Given the fitted value for C_e and σ_Δ, we can calculate the probability of each planet pair in resonance via two characteristic probability distribution functions (Eq. (2.19) and Eq. (2.20)): $P_{\mathrm{res},k} = p_{\mathrm{res}}(\Delta_{\mathrm{obs},k})/[p_{\mathrm{res}}(\Delta_{\mathrm{obs},k}) + p_{\mathrm{n-res}}(\Delta_{\mathrm{obs},k})]$. In Fig. 2.10, we plot the histogram of period ratio and resonance offset distribution of planet pairs weighted by $P_{\mathrm{res},k}$ (red hatches). It indicates the period ratio and resonance offset distribution of resonant pairs. The period ratio of resonant pairs peaks just wide of integer ratios, and, as the period ratio further increases, resonant pairs vanish. Not all pairs with period ratios close to integer ratio are in resonance.

The total number of resonant pairs is the summation of resonant probability over all

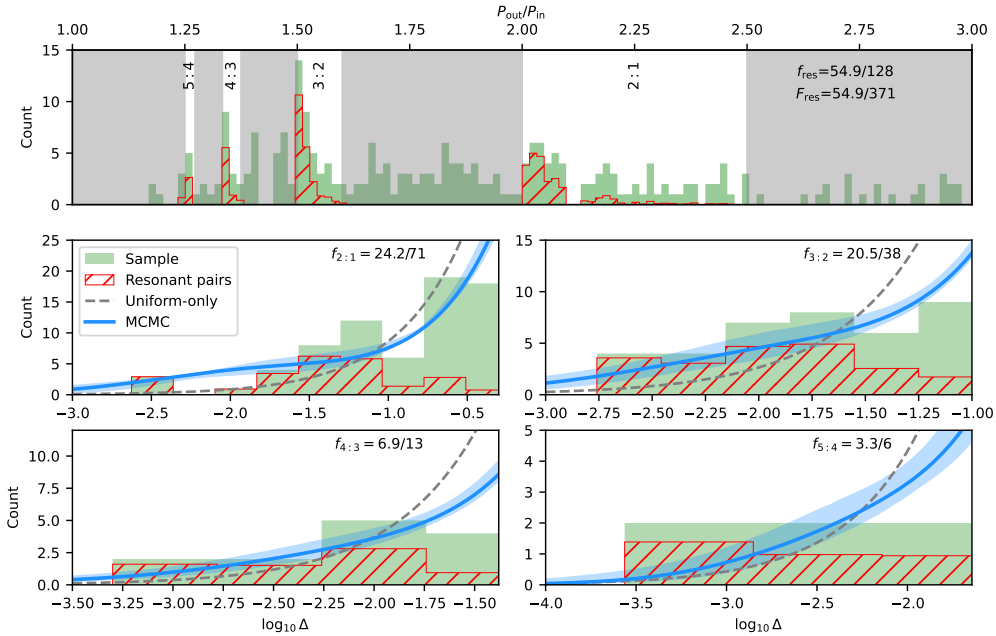

Figure 2.10. Distribution of period ratio (top panel, similar to Fig. 2.6) and resonance offset Δ (bottom panel) for the inferred resonant planet pairs (red hatches) versus all observed planet pairs in our sample (green histogram). The lower panels display the distribution of period ratio offset Δ within the highlighted four windows in the top panel. Grey dashed lines show the probability distribution of all planet pairs assuming they follow a uniform distribution (not in resonance). We compare it with the best MCMC fit result (blue curve, after bin size correction) assuming the Irradiated disc model. The shaded blue region indicates the 3σ uncertainty. We also label the fraction of inferred resonant planets, which is the ratio of the area between the red hatches and the green histograms (see Sect. 2.5.1 for details).

planet pairs:

$$N_{\rm res} = \sum_{k=1}^{N_{\rm pairs}} P_{{\rm res},k}. \tag{2.31}$$

We label the average fraction of resonant pairs, $f_{\rm res} = N_{\rm res}/N_{\rm pairs}$, on the top right of four lower panels in Fig. 2.10. $N_{\rm pairs}$ is the number of pairs in the narrow period ratio windows.

We also calculate the fraction of all resonant pairs among all pairs in our sample: $F_{\rm res} = N_{\rm res}/371 = 14.8^{+0.5}_{-0.7}\%$. The distribution is shown in Fig. 2.11 left panel. It is consistent with the crude estimation made by Wang & Ji (2014) (10%-20%). This number ignores higher-order resonances and first-order resonances with resonance numbers larger than 4 (5:4). The resonant fraction could therefore be higher.

We split the resonant planets into three groups, each group has a number of resonant pairs N_1, N_2, N_3, respectively, and $N_{\rm res} = N_1 + N_2 + N_3$ (see Sect. 2.2.5 for detail and Fig. 2.2 for a sketch). Three different resonant fractions are calculated:

- $f_{\rm res}({\rm Mig|out}) = N_1/(N_1 + N_2 + N_5)$: fraction of `Migrating` pairs among the pairs where the inner planets migrate slower than the outer;

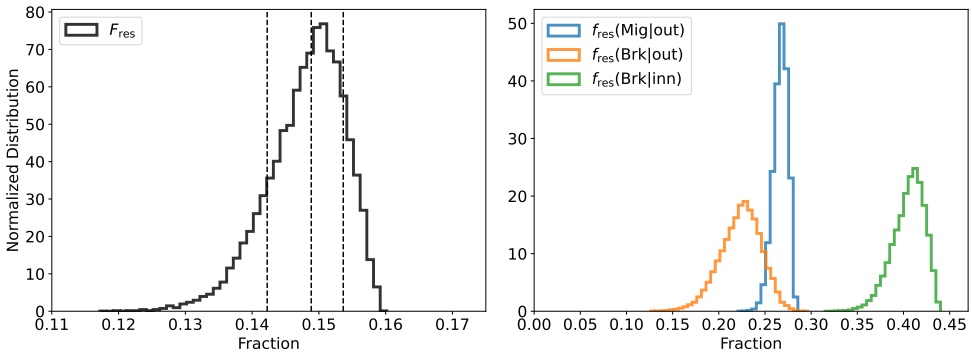

Figure 2.11. Resulting distribution of resonant fraction for all pairs in our sample (left) and detailed resonant distribution for pairs with period ratio within the near integer ratio windows (right). Here $f_{\rm res}$(Mig|out) is the fraction of planets that enter resonance during migration with the outer planet migrating faster. $f_{\rm res}$(Brk|out) is the fraction of resonant planets stopping at the disc inner edge with the outer planet migrating faster. $f_{\rm res}$(Brk|inn) is the fraction of resonant planets stopping at the disc inner edge with the inner planet migrating faster.

- $f_{\rm res}$(Brk|out) $= N_2/(N_1 + N_2 + N_5)$: fraction of `Braking` pairs among the pairs where the inner planets migrate slower than the outer;

- $f_{\rm res}$(Brk|inn) $= N_3/(N_3 + N_4)$: fraction of `Braking` pairs among the pairs where the inner planets migrate faster than the outer.

This classification allows us to compare the fraction of resonant pairs under different physical conditions. The distributions of the three fractions are shown in Fig. 2.11, right panel. It shows that $f_{\rm res}$(Mig|out) ≈ 0.27. This implies that in some pairs the ambient gas disc disperses before the pair reaches a migration barrier, i.e., either planet migration is slow or the disc disperses rapidly following planet migration and formation. The gas-poor formation scenario for sub-Neptunes (Dawson et al. 2015; Choksi & Chiang 2020) would be consistent with this picture. However, a still larger fraction of resonant pairs, $f_{\rm res}$(Brk|out) ≈ 0.23, and $f_{\rm res}$(Brk|inn) ≈ 0.41 reach their migration barriers. It implies that gas-poor formation applies to some of the observed systems, but not all of them. Interestingly, $f_{\rm res}$(Brk|out) is smaller than $f_{\rm res}$(Brk|inn), i.e., the inner planets tend to be more massive than the outers. A possible explanation would be that the inner edge of the disc – the location of the pressure maximum – would also be the place where pebbles accumulate. Pebble accretion at such locations can be very efficient (Chatterjee & Tan 2014; Jiang & Ormel 2023).

We also plot the eccentricity distribution for the planets in resonant pairs, weighted by their probability of being in resonance ($P_{{\rm res},k}$), in Fig. 2.12. Generally, the outer planets have smaller eccentricities consistent with Eq. (2.11). Their values mostly fall between 10^{-3} and 10^{-2}. It suggests that if we observe a sub-Neptune planet pair with relatively high eccentricities ($e \sim 0.1$), they are not likely to be in first-order resonance irrespective of their near-resonance period ratio. Post-disc perturbations (Choksi & Chiang 2022) could, however, excite eccentricities and change resonant pairs from apsidal anti-alignment to alignment (Laune et al. 2022). These apsidally aligned systems would have slightly larger eccentricities than what Fig. 2.12 predicts.

2.5.2 Upper limit on the disc surface density at resonance trapping

The constraints the MCMC model provides cannot be used to determine the absolute value of the natal disc surface density, as it cancels in the τ_a/τ_e expression. An upper limit for the natal disc surface density of resonant planets can, however, be deduced from the resonance trapping criterion. We use Eq. (2.26) in order to break the degeneracy and to find an upper limit for the disc surface density at the trapping location. It is assumed in the derivation of Eq. (2.26) that the outer planet is on a fixed circular orbit. Such an assumption is valid because the outer planets on average have lower eccentricities than their inner siblings (Fig. 2.12). From Sect. 2.4.2, we already found that $\tau_a/\tau_e > 10^3$ for observed transiting planets, that is, overstability is not likely to occur. In this regime, Eq. (2.26) alone gives the resonance trapping condition. Therefore, we can get the critical migration time-scale, below which the resonance would be crossed. In the Type I migration regime, planet migration speed is proportional to gas disc surface density. We are therefore able to obtain the upper limit of the disc gas surface density.

The upper limit is reached by combining Eq. (2.7), Eq. (2.9), Eq. (2.16) and Eq. (2.26):

$$\Sigma_{\max}(r_2) = 1.6|f_1|h^3(r_2)\left[(j+1)C_e\gamma_I\frac{\tau_{e_1}}{\tau_{e_2}}\right]^{\frac{1}{2}}\left(\frac{r_2M_1}{r_1M_2}\right)^{\frac{5}{4}}\frac{M_\star}{r_2^2} \tag{2.32}$$

inserting a disc model and extrapolating to 1 au, we obtain:

$$\begin{aligned}\Sigma_{\mathrm{1au,max}} =& 1.6|f_1|h_{\mathrm{1au}}^3\left[(j+1)C_e\gamma_I\right]^{1/2}\left(\frac{M_1}{M_2}\right)^{3/4}\\ &\times\left(\frac{r_1}{r_2}\right)^{2q-s/2-1.5}\left(\frac{r_2}{1\,au}\right)^{3q-s}\frac{M_\star}{r_2^2}.\end{aligned} \tag{2.33}$$

The expression $\Sigma_{\mathrm{1au,max}} \propto h_{\mathrm{1au}}^3$ is consistent with what Kajtazi et al. (2022) found in their simulations. In Fig. 2.13, we plot the $\Sigma_{\mathrm{1au,max}}$ for each planet pair that is possible in resonance, versus their host mass. The deeper the colour, the more likely it is that the pair is in resonance. The size of the symbol indicates the resonance index j. The figure shows that high-j resonances tend to be associated with high surface densities. This result is in line with Type-I migration theory. Massive discs result in faster migration, which allows the planets to cross the relatively strong resonance. In addition, Fig. 2.13 shows that $\Sigma_{\max}$ increases with stellar mass. That is because the migration speeds in the Type I limit depend on the star-to-disc mass ratio. Higher surface density is required to migrate faster. We indicate the surface density of the Minimum mass solar nebula (i.e., MMSN, Hayashi 1981) and the Minimum mass extra-solar nebula (i.e., MMEN, Chiang & Laughlin 2013) in Fig. 2.13. The upper limits of nearly all disc surface densities are below that of the MMEN, while the inferred disc surface densities are centred around the MMSN value.

We conclude this discussion with two final points. First, the value for $\Sigma_{\max}$ we obtained refers to the time when the planets were locked into resonance, not the upper limit over the entire disc lifetime. Second, planets in higher j resonances tend to provide higher upper limits on the disc surface density. However, they might alternatively have formed in close proximity to each other, avoiding crossing of lower-j resonances. In that case, the true value of Σ_{1au} is likely to be less than $\Sigma_{\mathrm{1au,max}}$.

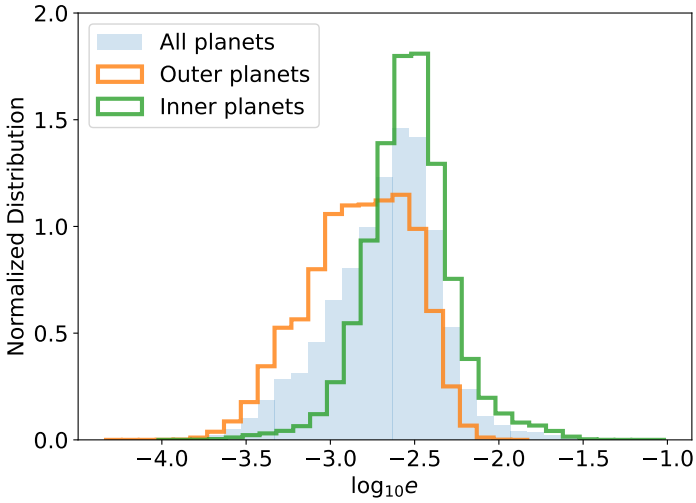

Figure 2.12. Eccentricity distribution of planet pairs that are in resonance, weighted by the probability of being in resonance. We compare the eccentricity distribution of the outer planets in all planet pairs with their inner planets.

2.5.3 Migration barrier reflects the disc inner rim

Planets can migrate in the disc, but their migration is believed to be halted somewhere as otherwise all planets would be consumed by the host star. However, the location and mechanism of the migration barrier are under debate. There are two main explanations for the barriers: dust sublimation (Kama et al. 2009; Flock et al. 2019) and the stellar magnetosphere (Königl et al. 2011; Hartmann et al. 2016).

If we assume a mass-luminosity relation for main sequence stars (Duric 2004), the dust sublimation radius becomes:

$$r_{\rm subl} = r_{\rm sub,0} \left(\frac{M_\star}{M_\odot}\right)^2, \tag{2.34}$$

where $r_{\rm sub,0}$ is the silicate dust sublimation radius for solar mass stars:

$$r_{\rm sub,0} = 0.13 \left(\frac{C_{\rm bw}}{1}\right)^{1/2} \left(\frac{0.1}{\epsilon}\right)^{1/2} \left(\frac{1400{\rm K}}{T_{\rm d}}\right)^2 {\rm au}, \tag{2.35}$$

where $C_{\rm bw}$ is the back-warming factor, ϵ is dust cooling efficiency and $T_{\rm d}$ is the dust sublimation temperature (Kama et al. 2009).

The magnetospheric infall radius tends to expand and converge to the stellar corotation radius due to angular momentum locking (Long et al. 2005). The stellar corotation radius is expressed as:

$$r_{\rm co} = 0.057 \left(\frac{P_\star}{5\,{\rm d}}\right)^{\frac{2}{3}} \left(\frac{M_\star}{M_\odot}\right)^{\frac{1}{3}} {\rm au} \tag{2.36}$$

The rotation periods of T Tauri stars (e.g. Bouvier et al. 2007; Lee & Chiang 2017) and young star associations (e.g.,Upper Sco and NGC 2264 Roquette et al. 2021) are several days (1-10 days).

The MCMC model is capable to identify (in a probabilistic sense) whether or not the planets have reached a migration barrier. We plot the location of the inner planet of those

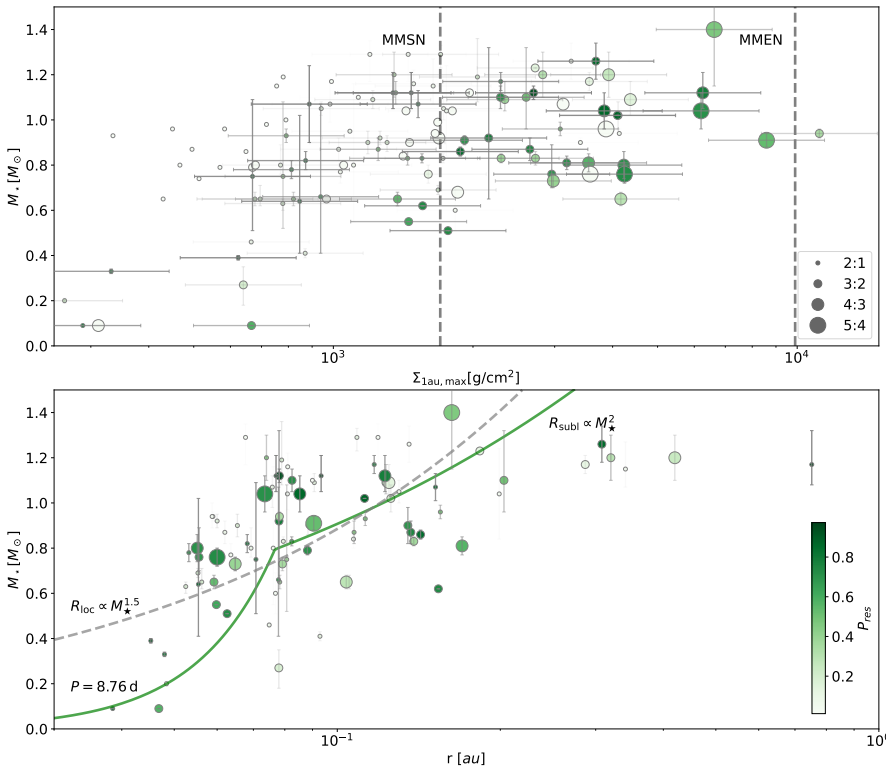

Figure 2.13. Inferred maximum surface density at 1 au for the resonant planets (top panel) and location of the migration barrier (bottom panel) versus the host stellar mass, for the 128 planet pairs in the four windows in Fig. 2.10. Different sizes of the circles indicate different resonance index j. The colour of the symbols indicates the probability of planets in resonance ($P_{\mathrm{res},k}$). In the top panel, error bars indicate the 1σ uncertainties in the stellar mass and $\Sigma_{1\mathrm{au,max}}$ – the latter follows from the uncertainty in C_e. The left and right grey dashed lines indicate the surface density of the MMSN and MMEN, respectively. In the bottom panel, grey and green lines give the best-fitting location of the migration barrier (the location of the inner planet in resonant pairs) fitted by a single power law and a broken power law, respectively.

pairs – the presumed location of the migration barrier – in Fig. 2.13. The symbol size again represents the resonance index j and the colour indicates how likely they are in resonance. From the plot, it can be seen that as the stellar mass increases the location of the migration barrier moves further away from the star. Motivated by the two theories about the migration barrier and aiming to figure out which radius is more consistent with observation, we fit the location of a migration barrier using the single power law expression:

$$r_{\mathrm{bar},k} = r_0 \left(\frac{M_{\star,k}}{M_\odot} \right)^l , \tag{2.37}$$

where r_0 is the location of the migration barrier for solar-mass stars. The Gaussian likelihood we construct is weighted by the resonance probability $P_{\mathrm{res},k}$:

$$\ln \mathcal{L} = \sum_{k=1}^{N_{\mathrm{pairs}}} \ln \left[\mathcal{N}(r_{\mathrm{bar},k} - r_k, \sigma_r^2) \cdot P_{\mathrm{res},k} \right] , \tag{2.38}$$

where $r_{\mathrm{bar},k}$, r_k and σ_r are the model predicted migration barrier location for the k-th pair (Eq. (2.37)), and the presumed location of the migration barrier and the standard deviation of the fitted migration barrier radius, respectively. If one pair has a larger $P_{\mathrm{res},k}$, it is more likely that the planets are formed in the protoplanet disc and undergo disc migration. The MLE fits $r_0 = 0.13$, $l = 1.49$ and σ_r is 0.079 au. The location of the migration barrier fitted by single power law relation is, however, shallower than the corresponding index of the dust sublimation radius but steeper than that of the magnetospheric radius. It may imply that there are two planet populations whose migration barriers are carved by either dust sublimation radius or magnetospheric radius. For this reason, we also fit a broken power law:

$$r_{\mathrm{bar},k} = \begin{cases} r_1 \left(\frac{M_{\star,k}}{M_\odot}\right)^{1/3} & \text{if } M_{\star,k} \leq M_{\mathrm{crit}} \\ r_2 \left(\frac{M_{\star,k}}{M_\odot}\right)^{2} & \text{if } M_{\star,k} > M_{\mathrm{crit}}, \end{cases} \tag{2.39}$$

where $M_{\mathrm{crit}} = (r_1/r_2)^{3/5} M_\odot$ is the transition mass between the two different power laws. Similar to the single power law, we use MLE to fit the two parameters $r_1 = 0.08$ au and $r_2 = 0.12$ au and the transition mass M_{crit} is $0.79 M_\odot$ (see Fig. 2.13). The low mass fit corresponds to a corotation period of $P_\star = 8.76$ days, which is consistent with the observed rotation period for young stars (Bouvier et al. 2007; Lee & Chiang 2017; Roquette et al. 2021). The value of r_2 agrees with Eq. (2.35). Around these high-mass stars, planets are trapped at the dust sublimation location as it exceeds r_{co}. However, the uncertainty $\sigma_r = 0.078$ au is only slightly smaller than the value given by the single power law, suggesting that the broken power law model is only marginally better. A larger sample will make for a more reliable analysis.

2.6 Discussion

In this work, we have constructed a model that connects the planet migration history to the observed values of the offset from integer period ratios (Δ). If the resulting planet pair is in resonance, Δ follows a log-normal distribution. On the other hand, if it is non-resonant, the corresponding Δ is assumed to follow a uniform distribution. Based on this, we have developed a statistical model that constrains the migration histories of the observed planets by conducting a Markov Chain Monte Carlo method (MCMC) analysis. We examine our MCMC method using self-generated mock data Sect. 2.B and prove that it can indeed reproduce certain features.

Our model for resonance trapping is designed for two-planet systems and first-order resonances, but we also include observed systems with planets in a resonance chain. Kajtazi et al. (2022) have shown that the averaged properties of the resonance chain (involving three or more planets) still reflect the properties of the system as if there is only one resonant pair. Therefore, multi-planet systems do not significantly contaminate the results. In addition, we have not considered higher-order resonances. A more general model that applies to both first-order and higher-order resonances needs to be considered in the future. Finally, it is possible that the inner planets migrate across the inner disc edge and enter the disc cavity (Huang & Ormel 2022; Fitzmaurice et al. 2022), where our model would not be applicable. But those planets are plausibly massive enough to open a deep gap (Ataiee & Kley 2021; Chrenko et al. 2022), which are excluded by our sample selection.

A key assumption in the model is that the uncertainties in the planet masses and the ensuing Δ follow a log-normal distribution. We can then fit the excess of period ratio just wide

of integer ratio with a log-normal profile, thus extracting pairs in resonance. If we would adopt different distributions for the mass, the resulting distributions for Δ would become far more complex and no longer allow us to express the corresponding likelihoods in closed form. However, certain post-disc dynamics, e.g., post-disc energy dissipation from planetesimal scattering (Chatterjee & Ford 2015; Ghosh & Chatterjee 2022), stellar tides (Lithwick & Wu 2012; Batygin & Morbidelli 2013) and stellar encounters (Cai et al. 2019; Stock et al. 2020), could slightly change the period ratios of planet pairs. Therefore, they may play roles in broadening, shifting, or even skewing the log-normal profile. What the resulting Δ distribution may look like needs to be investigated in future work. Once addressed, one may learn the post-disc perturbation histories the planets have experienced. However, this also requires a much larger sample size than what we have at present, as already in this work the MCMC is unable to break some model degeneracies.

Our model mainly applies to those small planets unable to open a gap (in Type I migration regime). Tanaka et al. (2002) and Tanaka & Ward (2004) showed that the semi-major axis damping time-scale (τ_a) and eccentricity damping time-scale (τ_e) have a relation for locally isothermal disc: $\tau_e = 1.28 C_e h^2 \tau_a/\gamma_I$ and $C_e = 1$. If the planet partially opens a gap, the migration speed decreases linearly with the gas surface density in the gap (Kanagawa et al. 2018). The same holds for eccentricity damping (Pichierri et al. 2022). Therefore, the ratio τ_a/τ_e is independent of surface density and the constraints we obtain on it still hold when the planet opens a partial gap. Neither assuming a specific disc nor migration model, we obtain that $\tau_a/\tau_e \approx 10^4$, which is the most robust result of this study. After adopting the irradiation disc model, we further obtain $C_e \approx 0.1$, which is consistent with one earlier statistics work Charalambous et al. (2022). We summarize three possible reasons for arriving at such a small C_e value in practice compared to locally isothermal migration theories (Tanaka et al. 2002; Tanaka & Ward 2004).

1. Mounting evidence increasingly suggests that Wind-driven accretion (Pascucci et al. 2023), plays a more prominent role as the primary mechanism of accretion, displacing the conventional notion of viscous accretion (Lynden-Bell & Pringle 1974). In scenarios where the disk's viscosity remains low Fedele et al. (2018), the predominant source of heating arises from stellar irradiation. Intriguingly, when the disk was optically thick, the disk aspect ratio could be lower ($h \lesssim 0.01$) than the irradiation model in our original paper where we assume an optically thin disk.

2. Post-disc dissipation mechanisms. Although we excluded planets with periods shorter than 5 days from our sample, tidal interactions (Lithwick et al. 2012; Batygin & Morbidelli 2013) may still be effective beyond this limit. Planetesimal scattering (Chatterjee & Ford 2015; Ghosh & Chatterjee 2022) and stellar encounters (Cai et al. 2019; Stock et al. 2020) are also important in shaping the final architecture of multi-planet systems. A more detailed evaluation of the mentioned interactions should be addressed in future studies.

3. Small γ_I ($\ll 1$). Non-isothermal prescription of γ_I was investigated in depth by Paardekooper et al. (2010, 2011). Very often at certain locations of the disc, planet migration can be effectively suppressed, i.e., $|\gamma_I| \ll 1$ (Baruteau et al. 2014; Benítez-Llambay et al. 2015). Planets can therefore stay at small eccentricities and large resonance offsets (Wang et al. 2021b).

Furthermore, by improving the analytical criterion for resonance trapping, we are able to constrain the upper limit on the natal disc surface density for those planets in resonance.

The resulting maximum surface density is similar to that of the Minimum Mass Solar Nebular (MMSN) but smaller than that of the Minimum Mass Extra-solar Nebula (MMEN).

Several other migration prescriptions have been proposed, including more sophisticated ones such as those by Paardekooper et al. (2010, 2011). These prescriptions demonstrate that planets within a certain mass range can be naturally trapped at a location where the (positive) corotation torque exerted on the planet exceeds the (negative) Lindblad torque (Bitsch et al. 2013, 2014; Baruteau et al. 2014). To first order, for small planets, the migration behavior would still be predominantly linear (with planet mass and disk mass) except near these trapping locations. In our model, such a scenario is naturally incorporated through the `Braking` pair. Regarding the dependence of the damping terms on planet eccentricity, non-linear correction terms have been proposed by e.g., Cresswell & Nelson (2006, 2008); Ida et al. (2020). However, at low eccentricity, these non-linear terms are irrelevant and we do not include these terms in our investigation. Finally, our findings on the ratio τ_a/τ_e are robust, irrespective of the specific disc migration prescriptions and non-linear terms. This is because this ratio has a one-to-one correspondence to the resonance offset Δ. Therefore, our conclusion regarding τ_a/τ_e remains valid even if we incorporate different migration models (disc structures) or non-linear terms.

The imprint resonant trapping leaves behind tentatively allow us to assess where and when planets form in the discs. The evaluation of the probability of planet pairs in MMR is crucial, and this step also informs us of the number of resonant pairs. Since we employ different models for how planets get trapped in resonance (Sect. 2.2.5), it is possible to distinguish gas-poor formation scenarios (pairs trapped in resonance when migrating) and gas-rich formation scenarios (pairs stopped by the migration barrier). The former could be identified with late formation, while the latter, which are more dominant, are connected to the early formation in gas-rich discs. The present orbits of these planets further hint at the location of migration barriers. However, due to our small sample, we cannot unambiguously identify the physical origin of the migration barrier; either the dust sublimation radius or the magnetospheric radius would fit the data. The situation is, however, expected to improve in the near future. The upcoming launch of the PLAnetary Transits and Oscillations of stars (PLATO) mission (e.g. Rauer et al. 2014) and The Earth 2.0 (ET) mission (Ge et al. 2022; Ye 2022) could drastically increase not only the number but also the precision of planet detections. It will provide us with a more precise analysis of the planet formation and migration histories reflected in the dynamical properties of resonant planets.

2.7 Conclusions

We manage to construct a statistical model connecting planet migration theory to observed quantities of Kepler planets. Based on the inferred masses and resonance offsets, we conduct an MCMC analysis to extract the history of planet-disc interaction from planet-planet dynamics. The statistical approach provides us with the following findings:

1. The semi-major axis-to-eccentricity damping time-scale ratio can be constrained at $\log_{10} \tau_a/\tau_e \approx 4$ with a dispersion of $\approx$0.3 dex, irrespective of the assumed disc model. The eccentricity damping is so efficient that overstable libration of resonances is unlikely to have occurred.

2. After assuming the isothermal irradiation disc, we obtain $\log_{10} C_e = -0.94^{+0.25}_{-0.25}$ which connects eccentricity damping and semimajor axis damping in the Type-I migration theory. This value is 10 times smaller than what was theoretically derived by Tanaka

et al. (2002) and Tanaka & Ward (2004) but in line with some recent analyses on individual multi-planet systems. The discrepancy could be attributed to our neglect of post-disk (tidal) damping effects or uncertainty in our understanding of disk migration.

3. From the MCMC posterior, the probability that a planet pair is in resonance follows. The fraction of transit planet pairs in first-order MMR amounts to $14.8^{+0.5}_{-0.7}\%$.

4. Most of the inferred resonant planets are consistent with the scenario that they reached a migration barrier, indicative of early migration in a gas-rich disc. The location of the migration barrier could be the dust sublimation radius for massive stars ($M_\star > 0.79 M_\odot$) and the magnetospheric radius for low mass stars ($M_\star < 0.79 M_\odot$).

5. By evaluating the resonance strength of those inferred resonant planets, the upper limit of the proto-disc surface density during the planet formation era is obtained. Most systems have their $\Sigma_{1\mathrm{au}}$ below that of the Minimum Mass Extra-solar Nebula (MMEN) and half of them below that of the Minimum Mass Solar Nebula (MMSN).

6. It is found that the classical MMR trapping/crossing criterion based on the pendulum model does not match numerical simulation. We provide and numerically verify an improved criterion (Eq. (2.26)) based on the equilibrium resonance angle, which together with the overstability condition of Goldreich & Schlichting (2014) (Eq. (2.30)) fully describes the problem.

Future work could feature a more complete model accounting for high-order resonances and resonance chains. Detection of more resonant planets and more precise measurements of planetary and stellar properties with upcoming missions will definitely improve the confidence of our analysis.

Appendix

2.A Results of the General disc model

The full MCMC fitting corner plot of the General model is shown in Fig. 2.14. The fitted values for all four parameters are $\log_{10}(C_e h_{1\mathrm{au}}^2) = -3.55^{+0.71}_{-0.89}$, $s = 1.58^{+0.58}_{-1.05}$, $q = 0.31^{+0.37}_{-0.47}$. However, these values do not necessarily refer to the real physical disc parameters, due to the degeneracy among them. Therefore, we generate mock planet period ratio data (with the same size as our sample used here) and examine this MCMC model without specifying the disc structure in Sect. 2.B.1. Those tests indeed suggest that s and q are not able to be retrieved.

Fig. 2.14 reveals the degeneracy: s negatively correlates with $\log_{10}(C_e h_{1\mathrm{au}}^2)$, q correlates positively with $\log_{10}(C_e h_{1\mathrm{au}}^2)$ and q positively with s. We found that such correlations are well represented by:

$$4q - s = C_2, \tag{2.40}$$

from Eq. (2.13) and

$$\log_{10}(C_e h_{1\mathrm{au}}^2) + 2q \log_{10} \frac{r_2}{1\,au} - \log_{10}(0.78\gamma_I) + (4q - s) \log \frac{r_1}{r_2} = C_1, \tag{2.41}$$

from Eq. (2.15), Eq. (2.14) and Eq. (2.16). C_1 and C_2 are two constants. Eq. (2.41) and Eq. (2.40) are indicated in Fig. 2.14 (green dashed lines), and they match the correlation. The fitted

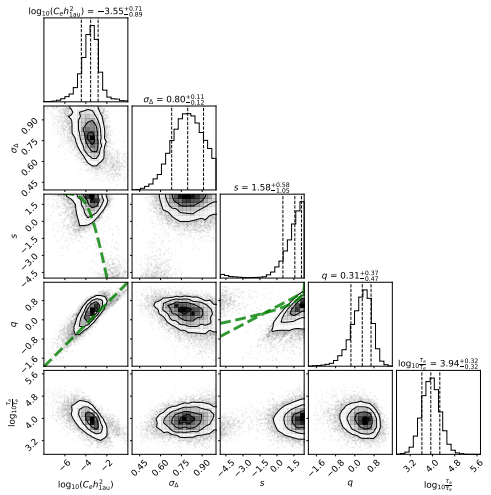

Figure 2.14. Corner plot of variables in the MCMC analysis ($\log_{10} C_e$, σ_Δ, s, and q) with 1σ, 2σ and 3σ confidence contours, w/o assuming the disc structure. We also calculate $\log_{10}(\tau_a/\tau_e)$ accordingly and add this variable into the corner plot. The 1σ uncertainty is labelled on the top of each column and indicated by left and right dashed lines. The middle dashed lines indicate their median values. Green lines indicate the correlation between different variables, which is Eq. (2.41) and Eq. (2.40).

log-normal dispersion σ_Δ, however, does not have any correlation with other parameters. It makes sense because our model does not depend on σ_Δ. We introduce another parameter:

$$\log_{10} \frac{\tau_a}{\tau_e} = \frac{C_e h(\overline{r}_1)^2}{0.78\gamma_I} \tag{2.42}$$

and it can be calculated given $\{\log_{10}(C_e h^2_{\rm 1au}), \sigma_\Delta, s, q\}$. Here, $\overline{r}_1$ is the observed semi-major axis of inner planet average over all planet pairs. This parameter is calculated and put in the corner plot. It shows that $\log_{10} \tau_a/\tau_e$ is a quantity independent of s and q, but slightly depends on $\log_{10}(C_e h^2_{\rm 1au})$.

2.B MCMC performance examination

As described in Sect. 2.4.1, we make use of planet masses, period ratios, semi-major axes and host masses from the NASA exoplanet database. Given these data as well as disc structure, we can then calculate the exact period ratios if planets are in resonance, and compare them to the observations. In this section, to examine the performance of the MCMC, we generate mock samples by replacing the actual period ratios with those assuming they are in or out of resonance. We randomly select a fraction of planet pairs to be in resonance and the fraction is $f_{\rm res}$. If they are not in resonance, the resulting period ratio follows a uniform distribution. If they are in resonance, the resulting period ratio is calculated via Eq. (2.12). We finally add log-normal noise to the planet masses with σ_m, which enables us to compare it to the resulting σ_Δ. In this way, the mock sample is generated, with known disc parameters. We then run the MCMC model to check whether we can reproduce the input parameters. The mock sample has the same size as the real sample we used in Sect. 2.4.

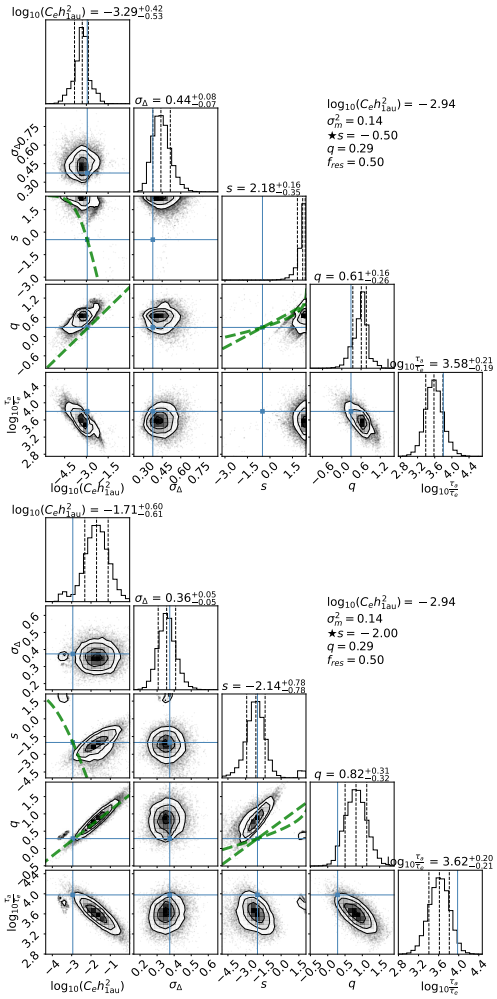

Figure 2.15. Similar to Fig. 2.14. Examination of MCMC model performance, without specifying the disc structure. In each panel, all parameters used are labelled in the upper right corner. We change the parameter s (labelled after ★) in different panels to examine the performance of MCMC model and we change s from -0.5 and -2. In each corner plot, blue lines show the true values. The 1σ uncertainty is labelled on the top of each column and indicated by left and right dashed lines. The middle dashed lines indicate their median values.

2.B.1 Tests without assuming a disc structure

We first examine whether the MCMC can reproduce $\log_{10}(C_e h^2_{\rm 1au})$, s and q, and whether the fitted σ_Δ is comparable to (the input) σ_m. Several sets of parameters are used for generating samples and model examination. The default parameters for generating the mock sample are $\log_{10}(C_e h^2_{\rm 1au}) = -2.94$, $\sigma_m = 0.374$, $s = -15/14$, $q = 2/7$ and $f_{\rm res} = 0.5$. We then test different values of s, q, and $f_{\rm res}$. The resulting corner plots are shown in Fig. 2.15, Fig. 2.16 and Fig. 2.17. The true value of parameters for generating mock samples is labelled at the top right of each panel and indicated by blue lines.

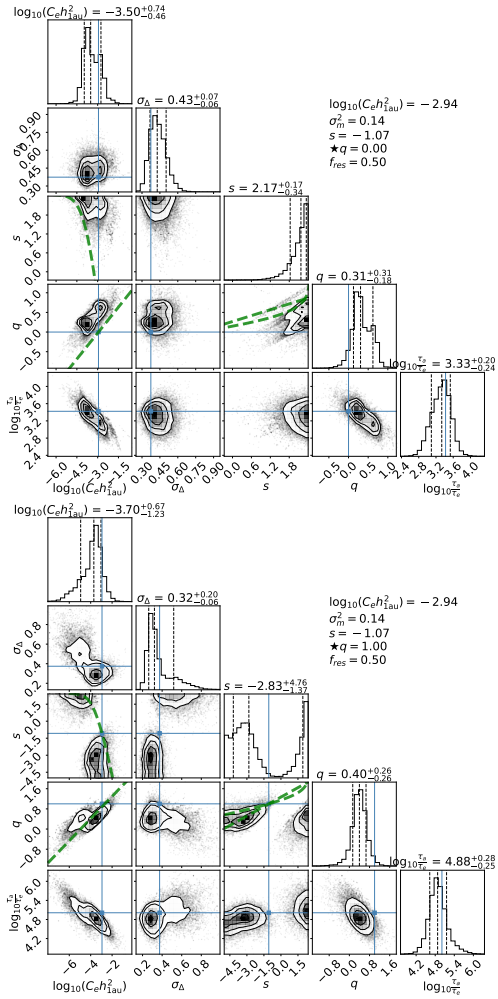

Figure 2.16. Similar to Fig. 2.15, but with different q. We change q from 0 and 1.

Unfortunately, the true values of $\log_{10}(C_e h^2_{1au})$, s and q are not properly retrieved. The posterior distribution gives the expected values for $\log_{10}(C_e h^2_{1au})$, s and q, but they are not consistent with the true values. However, the correlation between the parameters is revealed. The corner plot shows that s negatively correlates with $\log_{10}(C_e h^2_{1au})$, q is positively correlated to $\log_{10}(C_e h^2_{1au})$ and q is positively correlated to s. Their correlation is consistent with Eq. (2.41) and Eq. (2.40), indicated by green dashed lines.

Similar to Fig. 2.14, we also plot the posterior distribution of $\log_{10}(\tau_a/\tau_e)$ (Eq. (2.42)), which is a rather independent variable. The examination result suggests that $\log_{10}(\tau_a/\tau_e)$ can be fitted within 1.5σ error bar in all cases. The fitted σ_Δ is always very close to the log-normal error σ_m we impose for planet mass. It proves that the distribution of resonance offset Δ resulting from log-normal distributed planet masses also follows a log-normal distribution, when they are in resonance.

We therefore conclude that our MCMC model is useful for fitting $\log_{10}(\tau_a/\tau_e)$ but not $\log_{10}(C_e h^2_{1au})$, s and q if a disc structure has not been specified.

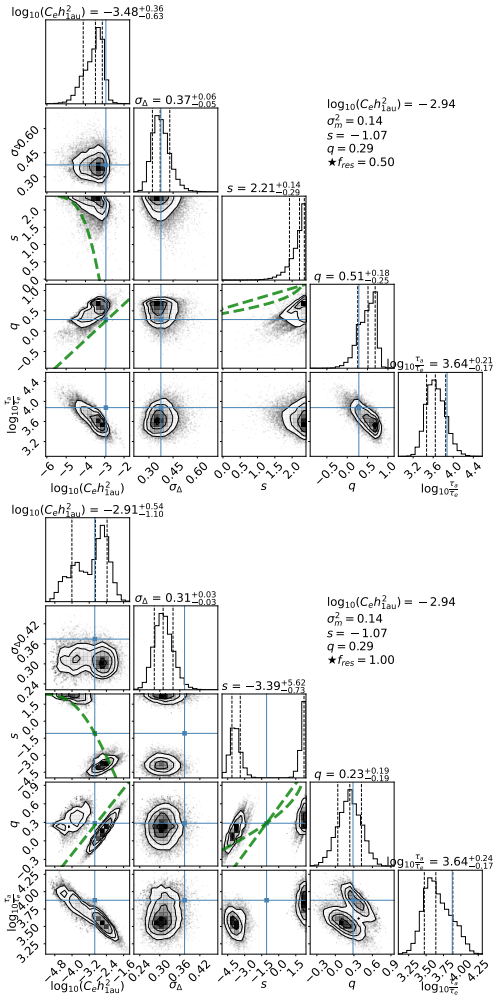

Figure 2.17. Similar to Fig. 2.15, but with different $f_{\rm res}$. We change fraction of pairs in resonance ($f_{\rm res}$) from 50% to 100%.

2.B.2 Tests assuming a disc structure

We here examine whether the MCMC can reproduce $\log_{10} C_e$, given a disc structure, and whether the fitted σ_Δ is still comparable to σ_m. We test several sets of parameters. The default parameter set is $\log_{10} C_e = 0.28$, $\sigma_m = 0.374$, $s = -15/14$, $q = 2/7$ and $f_{\rm res} = 0.5$. We then change each parameter to two other values, while keeping the other parameters the same.

The MCMC results are shown in Fig. 2.18. Different panels show the fit result for the mock sample generated from different parameter sets, and the true values of the parameters are labelled on the top right and indicated by blue lines. The true value of $\log_{10} C_e$ can always be reproduced within 1.5σ when $f_{\rm res} > 0.5$. The fitted σ_Δ is always consistent with σ_m as well. However, if we decrease the fraction of planets in resonance $f_{\rm res}$ to 0.1, the $\log_{10} C_e$ can no longer be retrieved and therefore the MCMC is no longer valid. However, when fitting

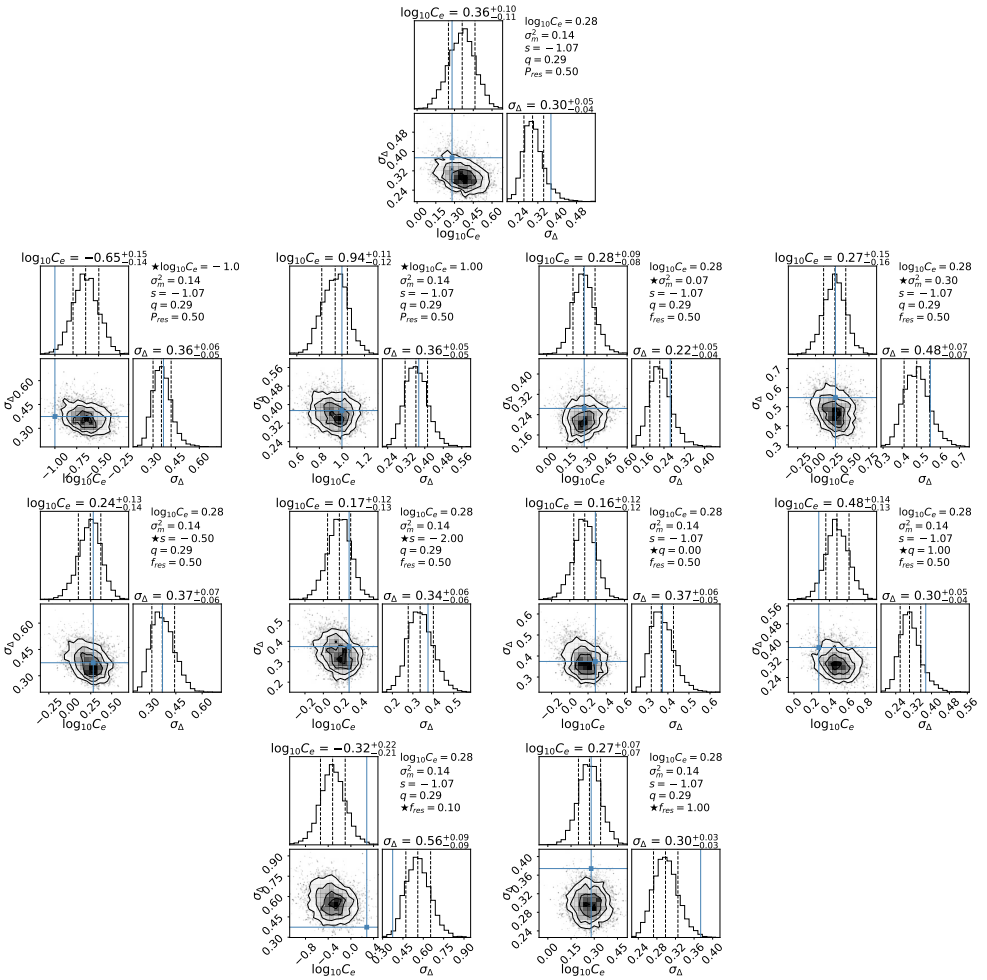

Figure 2.18. Examination of MCMC model performance, fixing the disc structure (the values of s and q). The top panel shows the fiducial model parameters. In each panel, all parameters used are labelled in the upper right corner. We then change every single parameter separately (labelled after ★) in each panel in the lower half of the figure. We change $\log_{10} C_e$ to -1, σ_m^2 to 0.07 and 0.3, s to -0.5 and -2, q to 0 and 1 and $f_{\rm res}$ to 10% and 100%. In each corner plot, blue lines show the true value of $\log_{10} C_e$ and $\sigma_{\rm m}$. The 1σ uncertainty is labelled on the top of each column and indicated by left and right dashed lines. The middle dashed lines indicate their median values.

the observed data, we have $f_{\rm res} \approx 0.5$ in most cases (Fig. 2.11 right panel). Therefore the MCMC results for the observed data are reliable.